# Endocytic regulation of cellular ion homeostasis controls lysosome biogenesis

Tania López-Hernández[1,3], Dmytro Puchkov[1], Eberhard Krause[1], Tanja Maritzen[1,3], Volker Haucke[1,2,3]

[1]*Leibniz-Forschungsinstitut für Molekulare Pharmakologie (FMP), 13125 Berlin, Germany.*

[2]*Freie Universität Berlin, Faculty of Biology, Chemistry, Pharmacy, 14195 Berlin, Germany.*

[3]*Corresponding authors: T.L.H. (lopezhernandez@fmp-berlin.de), T.M. (maritzen@fmp-berlin.de), V.H. (haucke@fmp-berlin.de).*

**Lysosomes serve as cellular degradation and signaling centers that coordinate metabolism in response to intracellular cues and extracellular signals. Lysosomal capacity is adapted to cellular needs by transcription factors, such as TFEB and TFE3, which activate the expression of lysosomal and autophagy genes. Nuclear translocation and activation of TFEB are induced by a variety of conditions such as starvation, lysosome stress, and lysosomal storage disorders. How these various cues are integrated remains incompletely understood. Here, we describe a pathway initiated at the plasma membrane that controls lysosome biogenesis via the endocytic regulation of intracellular ion homeostasis. This pathway is based on the exo-endocytosis of NHE7, a $Na^+$/ $H^+$ exchanger mutated in X-linked intellectual disability, and serves to control intracellular ion homeostasis and thereby $Ca^{2+}$/ calcineurin-mediated activation of TFEB and downstream lysosome biogenesis in response to osmotic stress to promote the turnover of toxic proteins and cell survival.**

Late endosomes, autophagosomes/ autolysosomes, and lysosomes coordinate degradative turnover of macromolecules with cell metabolism[1] by responding to intracellular cues (e.g. amino acid levels) and extracellular signals (e.g. insulin)[2, 3]. Lysosome dysfunction causes lysosomal storage diseases and neurodegeneration, while autophagy and lysosomal degradation have been shown to counteract pathologies ranging from cancer to Alzheimer's disease[4]. Adaptation of the autophagy/ lysosome pathway to changing environmental or internal cues is mediated in part by the coordinated expression of autophagic and lysosomal genes via the MiT-TFE family, most notably its founding member transcription factor EB (TFEB). While TFEB and its close relative TFE3 are kept sequestered in the cytosol under steady-state conditions, a

variety of stimuli have been shown to induce their nuclear translocation and activation. These include repression of mammalian target of rapamycin complex 1 (mTORC1) activity in starved cells[5], lysosome stress and lysosomal storage disorders[6, 7], physical exercise[8], and kinase-/ phosphatase-based signaling[3, 9, 10]. Nuclear translocation of TFEB and TFE3[7, 11] activates the expression of lysosomal and autophagy genes, thereby increasing the number of late endosomes, lysosomes and autophagosomes/ autolysosomes[6, 7, 12, 13] and, thus, the degradative capacity of cells.

Apart from the TFEB-based transcriptional network, lysosome function and biogenesis involve crosstalk with other organelles[14, 15]. For example, lysosomes receive membrane material from the biosynthetic pathway that delivers lysosomal membrane proteins and lumenal degradative enzymes to nascent lysosomes via vesicular carriers and from the plasma membrane via endocytic flux[15, 16]. At steady-state clathrin-mediated endocytosis (CME), a process that depends on clathrin, its main adaptor AP-2, and dynamin[17-19], represents a major entry portal for the delivery of plasma membrane proteins (e.g. signaling receptors) and lipids to the endolysosomal system[20]. Clathrin- and/ or dynamin-independent internalization pathways[21, 22] might also contribute to endocytic flux from the cell surface to lysosomes and autophagosomes/ autolysosomes. If and how exo-endocytic membrane dynamics affect lysosome and autophagosome biogenesis and how this may intersect with TFEB-based transcriptional responses to coordinately regulate the autophagy/ lysosome system remains poorly understood.

Here, we describe a pathway that is initiated at the plasma membrane and homeostatically controls lysosome and autophagosome biogenesis via endocytic regulation of intracellular ion homeostasis in response to osmotic stress to promote the turnover of toxic proteins and cell survival.

## Results

### Defective CME increases lysosome content via calcium-induced TFEB activation.

As endocytosis delivers membrane material to the endolysosomal system, we reasoned that inhibition of endocytosis might reduce lysosome content. We tested this hypothesis in mouse astrocytes by pharmacological inhibition of clathrin- and dynamin-dependent CME or by inhibition of clathrin-independent endocytic pathways (i.e. macropinocytosis, fast endophilin-mediated endocytosis) that depend on plasma membrane cholesterol, F-actin polymerization, and/ or class I phosphatidylinositol 3-kinase signaling[21, 22]. Surprisingly, we found that pharmacological blockade of CME by the dynamin inhibitor dynasore or the clathrin inhibitor Pitstop 2 led to the accumulation of late endosomes/ lysosomes containing lysosome-associated

membrane protein 1 (LAMP1) in primary astrocytes (Fig. 1a,b) or CD63 in HeLa cells (Extended Data Fig. 1a, Supplementary Data 1). Inhibition of phosphatidylinositol 3-kinase signaling by Wortmannin or GDC0941, F-actin polymerization by Cytochalasin D or the ARP2/3 inhibitor CK666, or cholesterol depletion by methyl-β-cyclodextrin were without effect (Fig. 1a,b; Extended Data Fig. 1a).

Lysosomal and autophagic gene expression are controlled in part by TFEB and TFE3, which undergo nuclear translocation in response to nutrient starvation, exercise, and other stimuli[6, 7, 12, 13, 23]. We hypothesized that the increase in the steady-state levels of lysosomes upon CME inhibition might be caused by TFEB/ TFE3 activation. Endogenous TFEB was cytoplasmic in control astrocytes, but accumulated in the nucleus of cells treated with dynasore or Pitstop 2 (Fig. 1c). This correlated with upregulated expression of lysosomal genes such as the vacuolar $H^+$-ATPase, the lysosomal $Ca^{2+}$ channel Mucolipin (MCOLN)/ transient receptor potential cation channel, mucolipin subfamily (TRPML) 1, and LAMP2 (Fig. 1d,e). Depletion of TFEB and TFE3 (Extended Data Fig. 1b-d) restored lysosomal gene expression in Pitstop 2- or dynasore-treated cells to normal levels (Fig. 1d,e). These data suggest that pharmacological blockade of CME induces lysosome biogenesis via TFEB/ TFE3. To challenge these unexpected findings by independent approaches, we analyzed the consequences of genetic perturbation of CME by siRNA-mediated knockdown (Supplementary Data 2 for illustration of general efficiency on the single cell level) of dynamin 2 (Extended Data Fig. 1e) or genomic ablation of the essential clathrin adaptor AP-2[24] in astrocytes derived from tamoxifen-inducible conditional AP-2μ knockout (KO) mice[25, 26] (Extended Data Fig. 1f). Akin to our observations in CME inhibitor-treated astrocytes, we found an accumulation of LAMP1-positive lysosomes in astrocytes depleted of dynamin 2 or deficient for AP-2μ (Fig. 1f-h, Extended Data Fig. 1g,h) and, hence, defective in CME (Extended Data Fig. 1i,j). In contrast, KO of the synaptotagmin adaptor Stonin 2[27] (Extended Data Fig. 1k), an endocytic protein dispensable for CME (Extended Data Fig. 1l,m), did not alter lysosome content (Fig. 1h; Extended Data Fig. 1n). Accumulation of LAMP1-positive lysosomes was also observed in other cell types (i.e. HeLa, Cos7, A431, SUM159pt, U-2 OS cells) depleted of AP-2μ (Extended Data Fig. 1o, Supplementary Data 3).

The late endosomal/ lysosomal GTPase Rab7[28], the lysosomal membrane protein LAMP2[16] and LC3-containing autophagosomes/ autolysosomes also accumulated in AP-2μ KO astrocytes. No changes in the levels or localization of early endosomal antigen 1 (EEA1), or the Golgi markers GM130, COPI, GGA3 were detectable (Extended Data Fig. 2a-d). Elevated cellular content of lysosomes, but not mitochondria in AP-2μ KO astrocytes was confirmed by electron microscopy (Extended Data Fig. 2e-g). AP-2μ KO astrocytes also displayed elevated

lysosomal cathepsin L activity (Extended Data Fig. 2h,i). Increased levels of lysosomes and autophagosomes/ autolysosomes were paralleled by nuclear translocation of TFEB in AP-2µ KO astrocytes (Fig. 1i,j; Extended Data Fig. 3a). Depletion of TFEB prevented the accumulation of Lysotracker- (Fig. 1k,l) or LAMP1-positive lysosomes (Extended Data Fig. 3b,c) and autophagosomes/ autolysosomes (Extended Data Fig. 3d,e), whereas elevated lysosome levels persisted in AP-2µ KO cells depleted of LAMP1 (Extended Data Fig. 3f-h), suggesting that lysosome accumulation is not a consequence of altered LAMP1 trafficking[15] in absence of AP-2. Re-expression of AP-2µ in KO astrocytes restored normal lysosome levels (Fig.1m; Extended Data Fig. 3i-l), further confirming the specificity of the phenotype.

TFEB activity is repressed by its mTORC1-dependent phosphorylation, while $Ca^{2+}$/ calcineurin-mediated dephosphorylation activates TFEB[29]. Loss of AP-2 did not cause a reduction of the levels of pAkt, a potent upstream activator of mTORC1, or of the mTORC1 substrates pmTORC1, pRaptor, pULK1, or pS6K1 (Extended Data Fig. 3m,n). AP-2µ KO astrocytes also did not display elevated levels of pPERK (Extended Data Fig. 4a), a mediator of ER stress that has been shown to induce TFEB/ TFE3 activation[30]. We therefore scrutinized the alternative possibility that TFEB activation might result from its increased dephosphorylation via calcineurin, potentially triggered by elevated cytosolic $Ca^{2+}$ levels in AP-2µ KO astrocytes. $Ca^{2+}$ imaging revealed a significant elevation of cytosolic $Ca^{2+}$ levels in AP-2µ KO astrocytes compared to WT controls (Fig. 2a,b). Sustained elevation of cytosolic $Ca^{2+}$ by thapsigargin-mediated release from ER $Ca^{2+}$ stores (Extended Data Fig. 4b,c) phenocopied loss of AP-2 with respect to the accumulation of lysosomes (Fig. 2c,d, Extended Data Fig. 4d,e), autophagosomes/ autolysosomes (Extended Data Fig. 4f,g), and nuclear translocation of TFEB (Extended Data Fig. 4h,i) in WT astrocytes. In AP-2µ KO astrocytes thapsigargin was without effect (Fig. 2c,d), suggesting that AP-2 loss and thapsigargin may converge on the same mechanism (e.g. $Ca^{2+}$). Sequestration of intracellular $Ca^{2+}$ by BAPTA-AM (Extended Data Fig. 4j,k) rescued the accumulation of lysosomes monitored by Lysotracker (Fig. 2e,f) or LAMP2 (Extended Data Fig. 4l,m), and the increase in LC3-II-positive autophagosomes/ autolysosomes (Extended Data Fig. 4n,o). Furthermore, blocking calcineurin activity by Cyclosporin A inhibition rescued lysosome accumulation in AP-2µ KO astrocytes (Fig. 2g,h, Extended Data Fig. 4p,q). Sequestration of cytosolic $Ca^{2+}$ by BAPTA-AM or calcineurin inhibition also blocked thapsigargin-induced lysosome biogenesis (Extended Data Fig. 4r, Supplementary Data 4). Elevated cytosolic $Ca^{2+}$ levels in AP-2µ KO cells could arise from extracellular $Ca^{2+}$ influx or via release from intracellular stores. No difference in steady-state lysosomal $Ca^{2+}$ levels was found between WT and AP-2µ KO astrocytes (Extended Data Fig. 5a,b). Moreover, loss of the lysosomal $Ca^{2+}$

channel Mucolipin/ TRPML1[1, 16] or depletion of inositol-triphosphate receptor type 2 ($IP_3R2$), the major $Ca^{2+}$ efflux pathway from the ER in astrocytes, did not affect lysosome accumulation in AP-2µ KO cells (Extended Data Fig. 5c-f). In contrast, scavenging extracellular $Ca^{2+}$ by EGTA rescued the increased lysosome biogenesis in AP-2µ KO astrocytes (Fig. 2i,j). Thus, defective CME in absence of AP-2µ induces lysosomal biogenesis via influx of extracellular $Ca^{2+}$, resulting in $Ca^{2+}$ /calcineurin-mediated activation of TFEB.

**Endocytosis of NHE7 controls ion homoestasis and lysosome biogenesis.**

We reasoned that loss of AP-2 in KO astrocytes might result in surface stranding of cycling membrane proteins, e.g. ion channels or exchangers, which may directly or indirectly affect cytosolic $Ca^{2+}$ levels. To identify such proteins, we devised a quantitative proteomics approach, in which biotinylated plasma membrane proteins were isolated from WT and KO astrocytes differentially labeled by stable isotope labeling by amino acids in cell culture (SILAC) (Fig. 3a; Extended Data Fig. 6a; Supplementary Table 5). We found the established CME cargo transferrin receptor (Fig. 3a, Extended Data Fig. 6b,c)[18, 19, 31] to accumulate on the surface of AP-2µ KO astrocytes, whereas the cell surface level of the plasma membrane-localized $Na^+$/ $K^+$-ATPase ATP1a1 was unchanged (Fig. 3a,b). Our attention was caught by the accumulation of several intracellular NHE proteins, most prominently the intracellular $Na^+$/ $H^+$-exchanger NHE7 (encoded by the gene Slc9a7) on the surface of AP-2µ KO astrocytes (Fig. 3a). In WT cells NHE7 is localized at the trans-Golgi network (TGN) and at early and recycling endosomes[32, 33](Extended Data Fig. 6d-i), suggesting that NHE7 may cycle via the plasma membrane. NHE7 is associated with cancer[33] and intellectual disability[34] and couples lumenal acidification to $Na^+$ export into the cytoplasm[32], thereby contributing to the regulation of intracellular ion homeostasis. We confirmed that loss of AP-2 causes the accumulation of NHE7 at the plasma membrane (Fig. 3b,d,e; Extended Data Fig. 6j,k) and elevated NHE7 protein levels (likely as a consequence of its impaired endocytosis and turnover over many days in KO cells) (Fig. 3b). Surface accumulation of NHE7 (>10-fold) was also overt when normalizing its cell surface pool to the increase in total NHE7 protein levels (Extended Data Fig. 6l). Depletion (Fig. 3c) or acute inhibition of dynamin (Extended Data Fig. 6n) also caused surface stranding of NHE7 substantiating defective endocytosis as the primary cause for its accumulation at the plasma membrane. Consistently, AP-2µ KO astrocytes displayed increased $Na^+$/ $H^+$ exchange activity (Fig. 3f,g), indicating that NHE7 is functionally active at the cell surface and facilitates $Na^+$ influx-coupled-$H^+$ export.

Hence, active NHE7 is likely retrieved from the cell surface by CME via complex formation with AP-2. We found a robust association of NHE7 with AP-2μ, while AP-2α/σ did not bind (Fig. 3h), suggesting that complex formation between AP-2 and NHE7 is mediated by tyrosine-based endocytic motifs. In agreement, NHE7 did not interact with an AP-2μ mutant defective in tyrosine motif recognition (Fig. 3h). AP-2, thus, retrieves NHE7 from the cell surface via tyrosine motif-dependent complex formation.

Based on these findings together with the observation that overexpression of NHE7 does not alter lysosome content in WT astrocytes (Extended Data Fig. 6m, Supplementary Data 5), we hypothesized that enhanced lysosome biogenesis in AP-2μ KO astrocytes is a consequence of altered ion homeostasis caused by surface stranding of active NHE7. In support, knockdown of NHE7 restored lysosomal gene transcription in dynasore-treated cells to normal levels (Extended Data Fig. 6o). Furthermore, depletion of NHE7 in AP-2μ KO astrocytes rescued the nuclear translocation of TFEB and the TFEB-mediated increase in lysosome (Fig. 3i-k; Extended Data Fig. 7a-e) and autophagosome/ autolysosome content (Extended Data Fig. 7f,g). Depletion of other transporters identified in our screen such as the intracellular NHE family member NHE6, an $H^+$-removing transporter that acts in reverse to NHE7[35], the plasma membrane localized $Na^+/H^+$ exchanger NHE1 and GLT-1, the major glutamate transporter in the brain, did not efficiently rescue elevated LAMP1 content in AP-2μ KO astrocytes (Extended Data Fig. 7h-m; Supplementary Data 6). AP-2-mediated endocytic retrieval of the $Na^+/ H^+$ exchanger NHE7 thus controls lysosome biogenesis.

NHE7 belongs to the conserved NHE family of $Na^+/ H^+$ exchangers that couple intracellular $Na^+$ homeostasis to pH regulation (Fig. 4a). Consistently, we found that AP-2μ KO astrocytes displayed a near twofold increase in cytosolic $Na^+$ levels compared to WT controls (Fig. 4b, Extended Data Fig. 8a). This was rescued by depletion of NHE7 (Fig. 4c, Extended Data Fig. 8b), suggesting that surface-stranded NHE7 causes $Na^+$ elevation. NHE7-mediated $Na^+$ influx might cause intracellular $Ca^{2+}$ overload via reduced $Ca^{2+}$ extrusion by the plasma membrane $Na^+/ Ca^{2+}$ exchanger NCX[36, 37](Fig. 4d; and below). We probed this hypothesis in several ways. Pharmacological elevation of cytosolic $Na^+$ levels by Ouabain, an inhibitor of the $Na^+/ K^+$-ATPase[38] phenocopied AP-2 loss in WT astrocytes with respect to lysosome accumulation (Fig. 4e,f), nuclear translocation of TFEB (Extended Data Fig. 8c,d), and induction of lysosomal gene expression (Extended Data Fig. 8e). Conversely, reduction of the extracellular $Na^+$ concentration to lower cytosolic $Na^+$ levels[38] rescued lysosome accumulation (Fig. 4g,h) and cytosolic $Ca^{2+}$ increase (Fig. 4i; Supplementary Data 7a) in AP-2μ KO astrocytes. Finally, depletion of NCX1 (Extended Data Fig. 8f), the most highly expressed NCX family member in

astrocytes[37] and a potential risk factor for neurodegeneration[39], rescued the elevation of cytosolic $Ca^{2+}$ levels (Fig. 4j; Supplementary Data 7b) as well as the increased biogenesis of lysosomes (Fig. 4k,l, Extended Data Fig. 8g,h) in AP-2μ KO astrocytes.

Collectively, our findings unravel a role for the $Na^+$/ $H^+$ exchanger NHE7 and the plasma membrane $Na^+$/ $Ca^{2+}$ exchanger NCX1 in the regulation of intracellular ion homeostasis that, in turn, controls the biogenesis of lysosomes and autophagosomes/ autolysosomes via TFEB (Fig. 4m,n).

**NHE7-induced lysosome biogenesis promotes toxic protein turnover.**

We reasoned that endocytic recycling of NHE7 to and from the plasma membrane must occur under physiological conditions in WT cells and could, thus, contribute to the regulation of lysosome and autophagosome biogenesis. Plasma membrane $Na^+$/ $H^+$ exchange via NHEs plays a crucial role in the adaptation of intracellular ion homeostasis and cell volume in response to hyperosmotic stress[40-42]. Hyperosmotic stress also profoundly affects the autophagy/ endolysosomal system by induction of autophagy[43, 44]. Autophagy and lysosomal proteolysis can remove protein aggregates formed under hyperosmotic conditions (due to reduced cell volume and elevated ionic strength caused by water efflux) and thereby counteract neurodegeneration[45, 46], e.g. in Parkinson's[47] or Huntington's disease[48]. We therefore hypothesized that the NHE7-TFEB/ TFE3 pathway may serve to induce autophagy/ lysosome biogenesis in response to hyperosmotic stress (Fig. 5a). Induction of hyperosmotic stress by application of mannitol indeed facilitated the activation and nuclear translocation of TFEB (Fig. 5b) resulting in the induction of lysosome and autophagy genes (Fig. 5c). Depletion of TFEB/ TFE3 (Extended Data Fig.9a) abrogated the induction of autophagy/ lysosomal gene (Fig. 5c) and protein (Extended Data Fig. 9b,c; Supplementary Data 8) expression in the presence of hyperosmotic mannitol, suggesting that TFEB/ TFE3 are critical for the cellular response to osmotic stress. Ultrastructural analysis by electron microscopy confirmed the elevated volume fraction of degradative organelles in mannitol-treated cells (Extended Data Fig. 9d). Closer inspection of these samples revealed a particularly prominent mannitol induction of early degradative late endosomal and autophagosomal profiles, while the content of electron dense late-stage lysosomes was unaltered (Fig. 5d-f; Extended Data Fig. 9e). This response was absent in mannitol-treated cells depleted of TFEB/ TFE3 (Fig. 5f; Extended Data Fig. 9f). Next, we probed the functional relevance of TFEB/ TFE3-induced lysosome and autophagosome biogenesis for the clearance of aggregated proteins in hyperosmotically stressed cells. Mannitol treatment induced protein aggregation visualized by Proteostat™, a reagent that detects aggregated forms of a large variety of

intracellular proteins (Fig. 5g,h). This was aggravated in TFEB/ TFE3-depleted cells (Fig. 5g,h). Similar results were seen for aggregates of pathogenic α-synuclein (Fig, 5i,j) causally involved in Parkinson's disease[46].

As hyperosmotic stress can also activate NHEs, we hypothesized that TFEB activation in mannitol-treated cells may be caused by the surface accumulation of NHE7. Indeed, we observed a significant increase of NHE7 at the plasma membrane of astrocytes treated with hyperosmotic mannitol (Fig. 6a,b). Hyperosmotic stress-induced surface enrichment of NHE7 may thus trigger TFEB/ TFE3-mediated lysosome and autophagsosome biogenesis. In support of this model, we found that knockdown of NHE7 prevented the induction of lysosome/ autophagy gene expression (Fig. 6c), nuclear translocation of TFEB (Extended Data Fig. 10b), and the resulting elevation of lysosome (Fig. 6d; Extended Data Fig. 10a; Supplementary Data 8) and autophagosome content (Fig. 6e; Extended Data Fig. 10c) in mannitol-treated cells. The induction of ultrastructurally discernible late endosomal and autophagosomal profiles by mannitol was also reduced (Fig. 6f; Extended Data Fig. 10d). The NHE7-TFEB/ TFE3 pathway may be important for the clearance of aggregated proteins, e.g. in neurodegenerative diseases and during aging, and thereby promote cell survival. Consistently, we observed that hyperosmotic mannitol increased the activity of lysosomal proteases such as cathepsin B, a response that was absent in astrocytes depleted of NHE7 (Fig. 7a,b). Moreover, loss of NHE7 promoted the accumulation of intracellular aggregates of endogenous proteins detected by Proteostat (Fig. 7c,d) or of expressed pathogenic α-synuclein (Fig. 7e,f) in hyperosmotically stressed cells. Finally, the accumulation of endogenous protein aggregates correlated with increased cell death under hyperosmotic conditions, a response that was further aggravated by depletion of NHE7 (Fig. 7g,h).

These findings delineate a prominent physiological function of NHE7-induced autophagy/ lysosome biogenesis via TFEB/ TFE3 in response to osmotic stress (Extended Data Fig. 10e).

## Discussion

We identify here a pathway for the TFEB/ TFE3-mediated induction of lysosome and autophagosome biogenesis that is based on the regulation of the endocytic recycling of NHE7, e.g. in response to hyperosmotic stress. We propose that the NHE7-TFEB pathway is part of an osmoprotective response that impinges on the transcriptional control of the autophagy/ lysosome system (e.g. via direct and/ or indirect effects of TFEB/ TFE3 on lysosomal gene expression[5]) This pathway, thus, adds a new facet to the range of physiological stimuli that regulate TFEB-

mediated lysosome and autophagosome biogenesis in response to various types of stresses[6-8, 23].

The precise molecular mechanisms by which alterations in osmolarity regulate NHE7 endocytosis are unclear at present. Hyperosmotic stress may conceivably disrupt the cycle of NHE7 exo- and endocytosis, either as a consequence of (i) impaired CME, a process known to be sensitive to hypertonic conditions[49], (ii) selective disruption of NHE7 complex formation with AP-2, e.g. due to posttranscriptional modifications such as phosphorylation[50], or (iii) increased NHE7 surface delivery. Further studies will need to test these possibilities.

As AP-2[18, 24, 51], NHE7, NCX1[52-54], as well as calcineurin and TFEB[12, 13] are broadly expressed, we expect the described pathway to be of importance in many cell types (consistent with Extended Data Fig. 1o) and tissues, especially in the brain. The prominent phenotypes caused by redistribution of NHE7 to the cell surface of astrocytes are consistent with the fact that the autophagy/ lysosome system is of particular importance in brain where it counteracts neurodegeneration[4, 55]. The brain is also especially vulnerable to changes in tonicity, and hyperosmotic stress is known to be associated with neurological pathologies. Moreover, osmotic stress is a potent protein aggregation stimulus in glial cells and a potential cause of osmotic demyelination syndrome (ODS)[56]. A key physiological function for the osmoprotective response induced by the NHE7-TFEB pathway in brain is further supported by identification of NHE7 as a risk gene for Alzheimer's disease[57]. Moreover, NHE7 has been found to be mutated in a familial form of X-linked mental retardation[34], while mutations in related endosomal NHE genes are linked to autism and other neurological disorders[58].

Unravelling the exact physiological roles of NHE7-induced lysosome biogenesis in brain and its potential dysfunction in neurological and neurodegenerative diseases may represent fruitful areas for future studies.

## References


1. Perera, R.M. & Zoncu, R. The Lysosome as a Regulatory Hub. *Annu Rev Cell Dev Biol* **32**, 223-253 (2016).
2. Dibble, C.C. & Cantley, L.C. Regulation of mTORC1 by PI3K signaling. *Trends Cell Biol* **25**, 545-555 (2015).
3. Saxton, R.A. & Sabatini, D.M. mTOR Signaling in Growth, Metabolism, and Disease. *Cell* **168**, 960-976 (2017).
4. Kollmann, K. *et al.* Cell biology and function of neuronal ceroid lipofuscinosis-related proteins. *Biochim Biophys Acta* **1832**, 1866-1881 (2013).

5. Settembre, C. *et al.* A lysosome-to-nucleus signalling mechanism senses and regulates the lysosome via mTOR and TFEB. *EMBO J* **31**, 1095-1108 (2012).
6. Perera, R.M., Di Malta, C. & Ballabio, A. MiT/TFE Family of Transcription Factors, Lysosomes, and Cancer. *Annu Rev Cancer Biol* **3**, 203-222 (2019).
7. Raben, N. & Puertollano, R. TFEB and TFE3: Linking Lysosomes to Cellular Adaptation to Stress. *Annu Rev Cell Dev Biol* **32**, 255-278 (2016).
8. Mansueto, G. *et al.* Transcription Factor EB Controls Metabolic Flexibility during Exercise. *Cell Metab* **25**, 182-196 (2017).
9. Li, Y. *et al.* Protein kinase C controls lysosome biogenesis independently of mTORC1. *Nat Cell Biol* **18**, 1065-1077 (2016).
10. Zoncu, R., Efeyan, A. & Sabatini, D.M. mTOR: from growth signal integration to cancer, diabetes and ageing. *Nature reviews. Molecular cell biology* **12**, 21-35 (2011).
11. Martina, J.A. *et al.* The nutrient-responsive transcription factor TFE3 promotes autophagy, lysosomal biogenesis, and clearance of cellular debris. *Sci Signal* **7**, ra9 (2014).
12. Sardiello, M. *et al.* A gene network regulating lysosomal biogenesis and function. *Science (New York, N.Y.)* **325**, 473-477 (2009).
13. Settembre, C. *et al.* TFEB links autophagy to lysosomal biogenesis. *Science (New York, N.Y.)* **332**, 1429-1433 (2011).
14. Bonifacino, J.S. & Traub, L.M. Signals for sorting of transmembrane proteins to endosomes and lysosomes. *Annu Rev Biochem* **72**, 395-447 (2003).
15. Janvier, K. & Bonifacino, J.S. Role of the endocytic machinery in the sorting of lysosome-associated membrane proteins. *Mol Biol Cell* **16**, 4231-4242 (2005).
16. Saftig, P. & Klumperman, J. Lysosome biogenesis and lysosomal membrane proteins: trafficking meets function. *Nature reviews. Molecular cell biology* **10**, 623-635 (2009).
17. Daumke, O., Roux, A. & Haucke, V. BAR domain scaffolds in dynamin-mediated membrane fission. *Cell* **156**, 882-892 (2014).
18. Kaksonen, M. & Roux, A. Mechanisms of clathrin-mediated endocytosis. *Nature reviews. Molecular cell biology* **19**, 313-326 (2018).
19. McMahon, H.T. & Boucrot, E. Molecular mechanism and physiological functions of clathrin-mediated endocytosis. *Nature reviews. Molecular cell biology* **12**, 517-533 (2011).
20. Bitsikas, V., Correa, I.R., Jr. & Nichols, B.J. Clathrin-independent pathways do not contribute significantly to endocytic flux. *Elife* **3**, e03970 (2014).

21. Boucrot, E. *et al.* Endophilin marks and controls a clathrin-independent endocytic pathway. *Nature* **517**, 460-465 (2015).
22. Mayor, S., Parton, R.G. & Donaldson, J.G. Clathrin-independent pathways of endocytosis. *Cold Spring Harb Perspect Biol* **6** (2014).
23. Puertollano, R., Ferguson, S.M., Brugarolas, J. & Ballabio, A. The complex relationship between TFEB transcription factor phosphorylation and subcellular localization. *EMBO J* **37** (2018).
24. Mitsunari, T. *et al.* Clathrin adaptor AP-2 is essential for early embryonal development. *Mol Cell Biol* **25**, 9318-9323 (2005).
25. Kononenko, N.L. *et al.* Retrograde transport of TrkB-containing autophagosomes via the adaptor AP-2 mediates neuronal complexity and prevents neurodegeneration. *Nat Commun* **8**, 14819 (2017).
26. Kononenko, N.L. *et al.* Clathrin/AP-2 mediate synaptic vesicle reformation from endosome-like vacuoles but are not essential for membrane retrieval at central synapses. *Neuron* **82**, 981-988 (2014).
27. Kononenko, N.L. *et al.* Compromised fidelity of endocytic synaptic vesicle protein sorting in the absence of stonin 2. *Proc Natl Acad Sci U S A* **110**, E526-535 (2013).
28. Zerial, M. & McBride, H. Rab proteins as membrane organizers. *Nature reviews. Molecular cell biology* **2**, 107-117 (2001).
29. Medina, D.L. *et al.* Lysosomal calcium signalling regulates autophagy through calcineurin and TFEB. *Nat Cell Biol* **17**, 288-299 (2015).
30. Martina, J.A., Diab, H.I., Brady, O.A. & Puertollano, R. TFEB and TFE3 are novel components of the integrated stress response. *EMBO J* **35**, 479-495 (2016).
31. Posor, Y. *et al.* Spatiotemporal control of endocytosis by phosphatidylinositol-3,4-bisphosphate. *Nature* **499**, 233-237 (2013).
32. Milosavljevic, N. *et al.* The intracellular Na(+)/H(+) exchanger NHE7 effects a Na(+)-coupled, but not K(+)-coupled proton-loading mechanism in endocytosis. *Cell Rep* **7**, 689-696 (2014).
33. Onishi, I. *et al.* Organellar (Na+, K+)/H+ exchanger NHE7 regulates cell adhesion, invasion and anchorage-independent growth of breast cancer MDA-MB-231 cells. *Oncol Rep* **27**, 311-317 (2012).
34. Khayat, W. *et al.* A recurrent missense variant in SLC9A7 causes nonsyndromic X-linked intellectual disability with alteration of Golgi acidification and aberrant glycosylation. *Hum Mol Genet* (2018).

35. Prasad, H. & Rao, R. The Na+/H+ exchanger NHE6 modulates endosomal pH to control processing of amyloid precursor protein in a cell culture model of Alzheimer disease. *J Biol Chem* **290**, 5311-5327 (2015).
36. Khananshvili, D. Sodium-calcium exchangers (NCX): molecular hallmarks underlying the tissue-specific and systemic functions. *Pflugers Arch* **466**, 43-60 (2014).
37. Pappalardo, L.W., Samad, O.A., Black, J.A. & Waxman, S.G. Voltage-gated sodium channel Nav 1.5 contributes to astrogliosis in an in vitro model of glial injury via reverse Na+ /Ca2+ exchange. *Glia* **62**, 1162-1175 (2014).
38. Lingrel, J.B. The physiological significance of the cardiotonic steroid/ouabain-binding site of the Na,K-ATPase. *Annu Rev Physiol* **72**, 395-412 (2010).
39. Sirabella, R. *et al.* NCX1 and NCX3 as potential factors contributing to neurodegeneration and neuroinflammation in the A53T transgenic mouse model of Parkinson's Disease. *Cell Death Dis* **9**, 725 (2018).
40. Garnovskaya, M.N., Mukhin, Y.V., Vlasova, T.M. & Raymond, J.R. Hypertonicity activates Na+/H+ exchange through Janus kinase 2 and calmodulin. *J Biol Chem* **278**, 16908-16915 (2003).
41. Grinstein, S., Woodside, M., Sardet, C., Pouyssegur, J. & Rotin, D. Activation of the Na+/H+ antiporter during cell volume regulation. Evidence for a phosphorylation-independent mechanism. *J Biol Chem* **267**, 23823-23828 (1992).
42. Nath, S.K. *et al.* Hyperosmolarity inhibits the Na+/H+ exchanger isoforms NHE2 and NHE3: an effect opposite to that on NHE1. *Am J Physiol* **270**, G431-441 (1996).
43. Nunes, P. *et al.* Hypertonic stress promotes autophagy and microtubule-dependent autophagosomal clusters. *Autophagy* **9**, 550-567 (2013).
44. Tamura, N., Kageyama, S., Komatsu, M. & Waguri, S. Hyperosmotic Stress Induces Unconventional Autophagy Independent of the Ulk1 Complex. *Mol Cell Biol* **39** (2019).
45. Fleming, A., Noda, T., Yoshimori, T. & Rubinsztein, D.C. Chemical modulators of autophagy as biological probes and potential therapeutics. *Nat Chem Biol* **7**, 9-17 (2011).
46. Sarkar, S. *et al.* Small molecules enhance autophagy and reduce toxicity in Huntington's disease models. *Nat Chem Biol* **3**, 331-338 (2007).
47. Fragniere, A.M.C. *et al.* Hyperosmotic stress induces cell-dependent aggregation of alpha-synuclein. *Sci Rep* **9**, 2288 (2019).
48. Chun, W., Lesort, M., Lee, M. & Johnson, G.V. Transient osmotic stress facilitates mutant huntingtin aggregation. *Neuroreport* **13**, 2543-2546 (2002).

49. Heuser, J.E. & Anderson, R.G. Hypertonic media inhibit receptor-mediated endocytosis by blocking clathrin-coated pit formation. *J Cell Biol* **108**, 389-400 (1989).
50. Hayashi, H., Szaszi, K. & Grinstein, S. Multiple modes of regulation of Na+/H+ exchangers. *Ann N Y Acad Sci* **976**, 248-258 (2002).
51. Robinson, M.S. Forty Years of Clathrin-coated Vesicles. *Traffic* **16**, 1210-1238 (2015).
52. Donowitz, M., Ming Tse, C. & Fuster, D. SLC9/NHE gene family, a plasma membrane and organellar family of Na(+)/H(+) exchangers. *Mol Aspects Med* **34**, 236-251 (2013).
53. Spugnini, E.P. *et al.* Proton channels and exchangers in cancer. *Biochim Biophys Acta* **1848**, 2715-2726 (2015).
54. Orlowski, J. & Grinstein, S. Diversity of the mammalian sodium/proton exchanger SLC9 gene family. *Pflugers Arch* **447**, 549-565 (2004).
55. Di Malta, C., Fryer, J.D., Settembre, C. & Ballabio, A. Astrocyte dysfunction triggers neurodegeneration in a lysosomal storage disorder. *Proc Natl Acad Sci U S A* **109**, E2334-2342 (2012).
56. Gankam-Kengne, F., Couturier, B.S., Soupart, A., Brion, J.P. & Decaux, G. Osmotic Stress-Induced Defective Glial Proteostasis Contributes to Brain Demyelination after Hyponatremia Treatment. *J Am Soc Nephrol* **28**, 1802-1813 (2017).
57. Meda, S.A. *et al.* A large scale multivariate parallel ICA method reveals novel imaging-genetic relationships for Alzheimer's disease in the ADNI cohort. *Neuroimage* **60**, 1608-1621 (2012).
58. Kondapalli, K.C., Prasad, H. & Rao, R. An inside job: how endosomal Na(+)/H(+) exchangers link to autism and neurological disease. *Front Cell Neurosci* **8**, 172 (2014).
59. Jordan, M., Schallhorn, A. & Wurm, F.M. Transfecting mammalian cells: optimization of critical parameters affecting calcium-phosphate precipitate formation. *Nucleic Acids Res* **24**, 596-601 (1996).
60. McCarthy, K.D. & de Vellis, J. Preparation of separate astroglial and oligodendroglial cell cultures from rat cerebral tissue. *J Cell Biol* **85**, 890-902 (1980).
61. Lange, S., Sylvester, M., Schumann, M., Freund, C. & Krause, E. Identification of phosphorylation-dependent interaction partners of the adapter protein ADAP using quantitative mass spectrometry: SILAC vs (18)O-labeling. *J Proteome Res* **9**, 4113-4122 (2010).
62. Cox, J. & Mann, M. MaxQuant enables high peptide identification rates, individualized p.p.b.-range mass accuracies and proteome-wide protein quantification. *Nat Biotechnol* **26**, 1367-1372 (2008).

**Acknowledgments.** We thank Sabine Hahn, Delia Löwe, Silke Zillmann and Claudia Schmidt for technical assistance, Drs. Mallorie Poet, David Owen, David Sabatini, Shawn Ferguson and David Rubinsztein for constructs, and Dr. Thomas Jentsch for discussion. Supported by the Deutsche Forschungsgemeinschaft (DFG, German Research Foundation) under Germany's Excellence Strategy (EXC-2049–390688087) and grants to V.H. (HA2686/13-1; Reinhart-Koselleck-Award).

**Author contribution.** T.L.H. performed all cell biological and biochemical experiments. D.P. carried out electron microscopy. E.K. conducted the quantitative proteomic analysis. T.L.H., T.M. and V.H. designed the study, analyzed data and wrote the manuscript with input from all authors.

**Author information.** The authors declare no competing financial interests. Correspondence and requests for materials should be addressed to V.H. (haucke@fmp-berlin.de), T.M. (maritzen@fmp-berlin.de) or T.L.H. (lopezhernandez@fmp-berlin.de).

**Data availability**

The data that support these findings are available from the authors on request. Statistical source data and unprocessed blots are provided as supplementary information.

**LEGENDS TO FIGURES**

**Figure 1| Accumulation of lysosomes upon block of clathrin-mediated endocytosis (CME)** **(a,b)** (a) WT astrocytes immunostained for LAMP1 after 15 h treatment with indicated inhibitors. Scale bars, 20 μm. (b) LAMP1 fluorescence intensity. Dashed line represents LAMP1 intensity of untreated cells. Data represent mean±SEM (N(dynasore)=5; N(other inhibitors)=6 independent experiments; one-way ANOVA with Tukey's post-test; **p(dynasore)=0.0033; ****p(Pitstop2)<0.0001; p(Wortmannin)=0.9992; p(GDC0941)=0.4797; p(CK666)=0.9886; p(CytochalasinD)>0.9999; p(MβDC)=0.9997). **(c)** Immunoblot of fractions from WT astrocytes treated with Pitstop2 or dynasore for 9 h. The experiment was repeated three times with similar results. **(d,e)** Gene expression analysis of WT astrocytes transfected with SCR or TFEB/TFE3-targeting siRNAs and treated or not with Pitstop2 (d) or dynasore (e) for 9 h. Bars show mRNA fold change normalized to GAPDH and relative to untreated cells. Data represent mean±SEM

((d) LAMP2/vATPase/MCOLN1: N(SCR;SCR+Pitstop2)=7/8/8 independent experiments; p=0.0038/0.0134/0.0027. (e) LAMP2/vATPase/MCOLN1: N(SCR;SCR+dynasore)=11/12/11; p=0.005/0.0158/0.0026. Two-sided one-sample t-test with Benjamini-Hochberg correction for multiple testing. (d) LAMP2/vATPase/MCOLN1: N(TFEB/TFE3KD+Pitstop2)=4/6/5; p=0.00356/0.0087/0.0105. (e) LAMP2/vATPase/MCOLN1: N(TFEB/TFE3KD+dynasore)=6/8/9; p=0.0103/0.0056/0.0289. Two-sided paired t-test). **(f-h)** Images of WT astrocytes transfected with SCR or dynamin2-targeting siRNAs (f) and of AP-2μ KO astrocytes (g) immunostained for LAMP1. Scale bars, 20 μm. (h) Quantification of LAMP1 fluorescence intensity. Values for controls were set to 1 (dashed line). Data represent mean±SEM (N(Dyn2 KD)=3; N(AP-2 KO)=8; N(STN2 KO)=2 independent experiments; two-sided one-sample t-test; *p(Dyn2)=0.048; ***p(AP-2)=0.0004). **(i,j)** (i) Images of WT and AP-2μ KO astrocytes immunostained for TFEB and AP-2α. Scale bar, 20 μm. (j) Quantification of fluorescence intensity of nuclear TFEB. WT values were set to 1. Data represent mean±SEM (N=5 independent experiments; two-sided one-sample t-test; *p=0.0192). **(k,l)** (k) Images of WT and AP-2μ KO astrocytes transfected with SCR or TFEB-targeting siRNAs and probed with Lysotracker. Scale bar, 20 μm. (l) Quantification of Lysotracker fluorescence intensity. Values were normalized to SCR-transfected WT astrocytes (dashed line) and represent mean±SEM (N=3 independent experiments; two-sided paired t-test; *p=0.0365). **(m)** Quantification of Lysotracker fluorescence intensity in AP-2μ KO astrocytes re-expressing AP-2μ and probed with Lysotracker. Values of non-transfected WT astrocytes were set to 1. Data represent mean±SD (N(untransfected WT astrocytes)=33; N(untransfected AP-2μ KO astrocytes)=46; N(AP- 2μ KO astrocytes rescued with AP-2μ)=42; 2 independent experiments; two-sided unpaired t-test; ****p<0.0001). a.u., arbitrary units; MβDC, methyl-β-cyclodextrin. See unprocessed blots in Source Data for Fig. 1.

**Figure 2 | $Ca^{2+}$/ calcineurin-mediated activation of TFEB promotes lysosome biogenesis upon loss of AP-2**

**(a,b)** (a) Images of WT and AP-2μ KO astrocytes incubated with the fluorescent $Ca^{2+}$ indicator Fluo-4-AM (Fluo4). Scale bar, 30 μm. (b) Quantification of Fluo4 fluorescence intensity. Data were normalized to WT and represent mean±SEM (N=10 independent experiments; two-sided one-sample t-test; ***p=0.0004). **(c,d)** (c) Representative confocal images of WT and AP-2μ KO astrocytes treated with DMSO or thapsigargin (TG) and immunostained for LAMP1. (d) Quantification of LAMP1 fluorescence intensity. Values were normalized to DMSO-treated WT astrocytes. Data represent mean±SEM (N=6 independent experiments; two-sided one-sample t-

test with Benjamini-Hochberg correction for multiple testing; *p(WT DMSO;WT TG)=0.016, **p(WT DMSO;KO DMSO)=0.0042). **(e,f)** (e) Images of AP-2µ KO astrocytes treated with DMSO or the cell-permeant $Ca^{2+}$ chelator BAPTA-AM and probed with Lysotracker. Scale bar, 20 µm. (f) Quantification of Lysotracker fluorescence intensity. Values were normalized to DMSO-treated WT astrocytes (illustrated by dashed line). Data represent mean±SEM (N=5 independent experiments; two-sided paired t-test; *p=0.015). **(g,h)** (g) LAMP1 immunostaining in AP-2µ KO astrocytes treated with DMSO or the calcineurin inhibitor Cyclosporin A. Scale bar, 20 µm. (h) Quantification of LAMP1 fluorescence intensity. Values were normalized to DMSO-treated WT astrocytes (illustrated by dashed line). Data represent mean±SEM (N=4 independent experiments; two-sided paired t-test; *p=0.0315). **(i,j)** (i) Images of AP-2µ KO astrocytes treated or not with EGTA and probed with Lysotracker. Scale bar, 20 µm. (j) Quantification of Lysotracker fluorescence intensity. Values were normalized to untreated WT astrocytes (illustrated by dashed line) and represent mean±SEM (N=5 independent experiments; two-sided paired t-test; **p=0.0012).

**Figure 3 | AP-2-mediated endocytic retrieval of the $Na^+$/ $H^+$ exchanger NHE7 controls lysosome biogenesis**

**(a-e)** (a) Cell surface proteins from WT and AP-2µ KO astrocytes were biotinylated and affinity-purified using streptavidin beads. The fold surface enrichment (=normalized ratio heavy/ light isotope labeled biotinylated samples) of select proteins in absence of AP-2 was quantified using a SILAC-based proteomics approach. Surface proteins from WT and AP-2µ KO astrocytes (b) or from WT astrocytes transfected with SCR or dynamin2 (Dyn2)-targeting siRNAs (c) were isolated like in (a). Total (input) and biotinylated proteins (surface) were analyzed by immunoblotting using antibodies against the indicated proteins. N-Cadherin and actin were used as markers for the membrane and cytosol fraction, respectively. The experiments were repeated twice with similar results. (d,e) Images of WT and AP-2µ KO astrocytes transfected with NHE7-GFP and immunostained for LAMP1 representative of 3 independent experiments with similar results. Scale bar, 20 µm. **(f,g)** (f) Average tracings for quantification in (g) illustrating the recovery of intracellular $pH_i$ after an extracellular $NH_4Cl$ pulse in WT and AP-2µ KO astrocytes. Data are mean±SD (N(WT)=58; N(KO)=44 astrocytes; 6 independent experiments). (g). Recovery of $pH_i$ presented as $\Delta pH_i/\Delta t$. Data are mean±SD (N(WT)=58; N(KO)=44 astrocytes; 6 independent experiments; two-sided unpaired t-test; ***p=0.0007). **(h)** Recombinant GST-AP-2µ WT, cargo-binding defective GST-AP-2µ mutant and GST-AP-2α/σ fusion proteins were immobilized on beads and incubated with extracts from NHE7-GFP-transfected HEK293 cells.

Eluted proteins were blotted and probed with GFP- and actin-specific antibodies. Representative of 3 independent experiments. **(i-k)** (i) Immunoblot analysis of nuclear fractionation of WT and AP-2µ KO astrocytes transfected with SCR or NHE7-targeting siRNAs. Nucleoporin p62 (NUP62) and GAPDH were used as markers for nuclear and cytosolic fraction, respectively. The experiment was repeated twice with similar results. (j) Images of WT and AP-2µ KO astrocytes transfected with SCR or NHE7-targeting siRNAs and immunostained for LAMP1. Scale bar, 20 µm. (k) Quantification of LAMP1 fluorescence intensity. Values for WT astrocytes transfected with SCR siRNA were set to 1 as illustrated by the dashed line. Data represent mean±SEM (N=10 independent experiments; two-sided paired t-test; ****p<0.0001). See unprocessed blots in Source Data for Fig. 3.

**Figure 4 | NHE7-mediated $Na^+$ influx induces $Ca^{2+}$ entry via the $Na^+$/ $Ca^{2+}$ exchanger NCX1 to trigger lysosome biogenesis**

**(a)** Scheme illustrating $Na^+$ concentrations and in-/efflux of $Na^+$. **(b)** Intracellular $Na^+$ concentration ($[Na^+]_i$) in AP-2µ KO astrocytes measured via the $Na^+$ sensor Asante NaTRIUM Green. Data represent mean±SEM (N=4 independent experiments; two-sided paired t-test; **p=0.0035). **(c)** Quantification of $[Na^+]_i$ in AP-2µ KO astrocytes transfected with SCR or NHE7-targeting siRNAs. Values represent mean±SD (N(WT/SCR)=159; N(KO/SCR)=201; N(KO/NHE7 siRNA)=199 astrocytes; 6 independent experiments; two-sided unpaired t-test; ****p<0.0001). **(d)** Scheme illustrating possible cause of elevated $[Ca^{2+}]_i$ in AP-2µ KO astrocytes. Application of Ouabain should phenocopy the increase in $[Ca^{2+}]_i$ by raising $[Na^+]_i$. **(e,f)** (e) Images of WT astrocytes treated with DMSO or Ouabain and immunostained for LAMP1. Scale bar, 20 µm. (f) LAMP1 fluorescence intensity values were normalized to DMSO-treated astrocytes. Data represent mean±SEM (N=3 independent experiments; two-sided one-sample t-test; *p=0.0159). **(g-i)** (g) Images of WT and AP-2µ KO astrocytes incubated extracellularly with 155 mM or 30 mM $Na^+$ and immunostained for LAMP1. Scale bar, 20 µm. (h) LAMP1 fluorescence intensity values were normalized to WT astrocytes incubated with 155 mM $Na^+$ (dashed line) and represent mean±SEM (N=6 independent experiments; two-sided paired t-test; *p=0.0467). (i) Recovery of elevated intracellular $Ca^{2+}$ in AP-2µ KO astrocytes incubated extracellularly with 30 mM $Na^+$ and probed with the $Ca^{2+}$ sensor Fluo8. Fluo8 fluorescence intensity values were normalized to WT astrocytes incubated with 155 mM $Na^+$ (dashed line) and represent mean±SD (N(WT 155 mM $Na^+$)=341; N(AP-2µ KO 155 mM $Na^+$)=307; N(AP-2µ KO 30 mM $Na^+$)=366 astrocytes; 3 independent experiments; two-sided unpaired t-test; ****p<0.0001). **(j)** WT and AP-2µ KO astrocytes transfected with SCR or

NCX1-targeting siRNAs were incubated with Fluo8. Fluo8 fluorescence intensity values were normalized to WT astrocytes transfected with SCR siRNA (dashed line). Data represent mean±SEM (N=4 independent experiments; two-sided paired t-test; *p=0.0339). **(k,l)** (k) Images of WT and AP-2µ KO astrocytes transfected with SCR or NCX1-targeting siRNAs and probed with Lysotracker. Scale bar, 20 µm. (l) Lysotracker intensity values were normalized to WT astrocytes transfected with SCR siRNA (dashed line). Data represent mean±SEM (N=4 independent experiments; two-sided paired t-test; *p=0.022). **(m,n)** Scheme illustrating the role of AP-2 (m) and the consequence of its loss (n).

**Figure 5 | Hyperosmotic stress induces TFEB activation required for cell adaptation**

**(a)** Scheme of NHE7´s role in adaptation. **(b,c)** (b) Immunoblot analysis (representative of 3 independent experiments) of nuclear fractionation of WT astrocytes treated with mannitol for 5 h. (c) Expression analysis of lysosomal and autophagy genes in WT astrocytes transfected with SCR or TFEB/TFE3-targeting siRNAs and treated or not with mannitol for 5 h. Bars show the mRNA fold change normalized to GAPDH and relative to untreated cells. Data represent mean±SEM (LAMP2/LAMP1/vATPase/LC3: N(SCR;SCR+Mannitol)=8/7/8/8 independent experiments, p=0.0654/0.0162/0.0015/0.0342; N(TFEB/TFE3 KD)=7/6/7/7, p=0.9614/0.4992/0.579/0.9472; N(TFEB/TFE3 KD+mannitol)=8/6/8/8, p=0.9614/0.0702/0.2778/0.9472; two-sided one-sample t-test with Benjamini-Hochberg correction for multiple testing). **(d-f)** Representative electron micrographs reveal accumulation of early degradative structures (green) in astrocytes treated with mannitol for 5 h. Nuclei in blue. Scale bar, 2 µm. Black boxes in (d) represent magnified areas shown in (e). Scale bar, 1 µm. (f) Quantification of volume fraction of late endosomes and autophagic vacuoles present in EM images of WT astrocytes transfected with SCR or TFEB/TFE3-targeting siRNAs and treated or not with mannitol. Data represent mean±SEM (N(SCR)=33; N(SCR+mannitol)=23; N(TFEB/TFE3 KD+mannitol)=17 astrocytes; 2 independent experiments; one-way ANOVA with Tukey's post-test; ****p(SCR;SCR+mannitol)<0.0001; **p(SCR+mannitol;TFEB/TFE3 KD+mannitol)=0.0019). **(g-h)** (g) Images of WT astrocytes transfected with SCR or TFEB/TFE3-targeting siRNAs, treated or not with mannitol for 24 h and probed with Proteostat. Scale bar, 20 µm. White boxes, zoom of the marked area. Scale bar, 10 µm. (h) Quantification of the relative number of protein aggregates. Values were normalized to untreated WT astrocytes transfected with SCR siRNA. Data represent mean±SEM (N(SCR; SCR+mannitol)=8; N(TFEB/TFE3 KD)=4; N(TFEB/TFE3 KD+mannitol)=5 independent experiments; two-sided one sample t-test with Benjamini-Hochberg correction for multiple testing for comparison of

611 treated and non-treated SCR transfected astrocytes (**p=0.0012) and two-sided paired t-test for
612 comparison of mannitol-treated astrocytes (*p=0.0164)). **(i,j)** (j) Images of WT astrocytes
613 transfected with SCR or TFEB/TFE3-targeting siRNAs and the mutant variant A53T of α-
614 synuclein (GFP-A53Tα-syn) treated or not with mannitol for 24 h. Scale bar, 20 μm. White
615 boxes, zoom of the marked area. Scale bar, 10 μm. (h) Quantification of the number of GFP-
616 A53Tα-syn protein aggregates. Data represent mean±SEM (N(SCR;SCR+mannitol)=10;
617 N(TFEB/TFE3 KD;TFEB/TFE3 KD+mannitol)=4 independent experiments; one-way ANOVA
618 with Tukey's post-test; ****p(SCR;SCR+mannitol)<0.0001;
619 ****p(SCR+mannitol;TFEB/TFE3KD+mannitol)<0.0001). See unprocessed blots in Source
620 Data for Fig. 5.
621
622 **Figure 6 | NHE7 activity is required for hyperosmotic stress-induced TFEB activation**
623 **(a,b)** (a) Cell surface proteins from WT astrocytes treated with mannitol for 1 h were
624 biotinylated and affinity-purified by streptavidin beads. Total (input) and biotinylated proteins
625 (surface) were analyzed by immunoblotting. (b) Quantification of NHE7 surface levels. Values
626 for untreated astrocytes were set to 1. Data represent mean±SEM (N=9 independent experiments;
627 two-sided one-sample t-test; *p=0.0473). **(c)** Expression analysis of TFEB target genes in WT
628 astrocytes transfected with SCR or NHE7-targeting siRNAs and treated or not with mannitol for
629 5 h. Bars show the mRNA level fold change normalized to the housekeeping gene GAPDH and
630 relative to the untreated cells. Data represent mean±SEM (LAMP2/LAMP1/vATPase/LC3:
631 N(SCR;SCR+Mannitol)=15/17/13/15 independent experiments,
632 p=0.0003/0.0003/0.0018/0.0006; N(NHE7 KD)=11/11/8/10, p=0.8377/0.863/0.221/0.6116;
633 N(NHE7 KD+mannitol)=12/13/9/11, p=0.65865/0.3055/0.077/0.3958; two-sided one-sample t-
634 test with Benjamini-Hochberg correction for multiple testing). **(d-f)** (d) Quantification of
635 LAMP1 fluorescence intensity in WT astrocytes transfected with SCR or NHE7-targeting siRNA
636 and treated or not with mannitol for 5 h. Values for untreated astrocytes transfected with SCR
637 siRNA were set to 1. Data represent mean±SEM (N(SCR;SCR+mannitol)=11; N(NHE7 KD)=7,
638 N(NHE7 KD+mannitol)=8 independent experiments; two-sided one sample t-test with
639 Benjamini-Hochberg correction for multiple testing for comparison of treated and non-treated
640 SCR transfected astrocytes (**p=0.0012) and two-sided paired t-test for comparison of mannitol-
641 treated astrocytes (*p=0.0110)). (e) Quantification of relative LC3-II/β-actin ratio of
642 immunoblots of cell lysates from WT astrocytes transfected with SCR or NHE7-targeting
643 siRNAs and treated or not with mannitol for 5 h. Values for untreated astrocytes transfected with
644 SCR siRNA were set to 1. Data represent mean±SEM (N=5 independent experiments; two-sided

one sample t-test for comparison of treated and non-treated SCR transfected astrocytes (*p=0.0462) and two-sided paired t-test for comparison of mannitol-treated astrocytes (*p=0.0257)). (f) Quantification of volume fraction of late endosomes and autophagic vacuoles present in EM images of WT astrocytes transfected with SCR or NHE7-targeting siRNAs and treated or not with mannitol for 5 h. Data represent mean±SEM (N(SCR)=33; N(SCR+mannitol)=23; N(NHE7 KD+mannitol)=30 astrocytes; 2 independent experiments; one-way ANOVA with Tukey's post-test; ****p(SCR;SCR+mannitol)<0.0001; **p(SCR+mannitol;TFEB/TFE3 KD+mannitol)=0.002). See unprocessed blots in Source Data for Fig. 6.

**Figure 7 | Pro-survival role of NHE7 activity for adapting lysosome function in cells subjected to hyperosmotic stress**

**(a,b)** (a) *In vivo* proteolytic activity of Cathepsin B was assayed by incubation with Magic Red. Images of WT astrocytes transfected with SCR or NHE7-targeting siRNAs and treated or not with mannitol for 5 h. Scale bar, 20 μm. (b) Magic Red fluorescence intensity values for untreated WT astrocytes were set to 1. Data represent mean±SEM (N=3 independent experiments; two-sided one sample t-test with Benjamini-Hochberg correction for multiple testing for comparison of treated and non-treated SCR transfected astrocytes (*p=0.01335) and two-sided paired t-test for comparison of mannitol-treated astrocytes (*p=0.0216)). **(c,d)** (c) Images of WT astrocytes transfected with SCR or NHE7-targeting siRNAs, treated or not with mannitol for 24 h and probed with Proteostat. Scale bar, 20 μm. White boxes, zoom of the marked area. Scale bar, 10 μm. (d) Quantification of the relative number of protein aggregates. Values were normalized to untreated WT astrocytes transfected with SCR siRNA. Data represent mean±SEM (N(SCR;SCR+mannitol)=9; N(NHE7 KD)=3; N(NHE7 KD+mannitol)=5 independent experiments; two-sided one-sample t-test with Benjamini-Hochberg correction for multiple testing for comparison of treated and non-treated SCR transfected astrocytes (***p=0.0006) and two-sided paired t-test for comparison of mannitol-treated astrocytes (**p=0.0037). **(e,f)** (e) Images of WT astrocytes transfected with SCR or NHE7-targeting siRNAs and the mutant variant A53T of α-synuclein (GFP-A53Tα-syn) treated or not with mannitol for 24 h. Scale bar, 20 μm. White boxes show a zoom of the marked area. Scale bar, 10 μm. (f) Quantification of the number of GFP-A53Tα-syn protein aggregates. Data represent mean±SEM (N(SCR;SCR+mannitol)=10; N(NHE7 KD)=5; N(NHE7 KD+mannitol)=6 independent experiments; one-way ANOVA with Tukey's post-test; ****p(SCR;SCR+mannitol)<0.0001; ***p(SCR+mannitol;NHE7 KD+mannitol)=0.0004). **(g,h)**

679 (g) Images of WT astrocytes transfected with SCR or NHE7-targeting siRNAs treated or not for
680 24 h with mannitol and immunostained for active (=cleaved) caspase3. The nuclei were stained
681 by DAPI (blue). Scale bar, 50 μm. (h) Quantification of % cells with immunostaining for active
682 caspase3. Data represent mean±SEM (N(SCR;SCR+mannitol)=12; N(NHE7 KD)=4; N(NHE7
683 KD+mannitol)=9 independent experiments; one-way ANOVA with Tukey's post-test;
684 ***p(SCR;SCR+mannitol)=0.001; *p(SCR+mannitol;NHE7 KD+mannitol)=0.0466). See in
685 Source Data for Fig. 7.

## Methods

### Plasmids

Human NHE7 cDNA in a pIRESHyg3 vector (described in[32]) was a kind gift from Mallorie Poet (Université Nice Sophia Antipolis, France). NHE7 cDNA was subcloned into pEGFP-N1 for expression of C-terminally EGFP-tagged NHE7. For rescue experiments, we used a construct containing murine untagged AP-2μ followed after an IRES site by mRFP in an adenoviral AAV-HBA-EWB vector backbone. Plasmids encoding GST-AP-2μ WT (aa157-435 in pGEX4T-1) and (D176A/W421A) as well as GST-tagged AP-2α co-expressed with untagged AP-2σ to obtain AP-2α/σ hemicomplexes have been described before. pGFPP-N1-TFEB was a gift from Shawn Ferguson (Addgene plasmid #38119; http://n2t.net/addgene:38119; RRID:Addgene_38119). The plasmid encoding EGFP-alphasynuclein-A53T was a gift from David Rubinsztein (Addgene plasmid #40823; http://n2t.net/addgene:40823 ; RRID:Addgen_40823).

### siRNAs

siRNA oligonucleotides used in this study (SMART pools consisting of 4 siRNAs) are listed in Supplementary Table 1.

### Antibodies

*Immunoblotting:* Secondary antibodies were in all cases species-specific. HRP-conjugated or LI-COR 800CW and 680RD infrared suitable antibodies were applied at 1:10,000 in blocking solution. Quantification was done based on chemiluminescence or fluorescence using the Odyssey FC detection system. Each panel of a figure has individual antibodies shown at the same exposure settings throughout the experiment.

*Immunofluorescence:* Secondary antibodies were in all cases species-specific. Secondary antibodies fluorescently labeled with Alexa dyes 488, 568 or 647 (Thermo Fisher Scientific) were applied at 1:300 in blocking solution.

Antibodies used in this study are listed in Supplementary Table 2.

### Drugs and chemicals

Drugs and chemicals used in this study are provided in Supplementary Table 3.

### DNA transfections and siRNA knockdowns

HeLa, HEK293T, Cos7, A431, Sum159pt and U-2 OS cells were transfected with siRNAs at 50 nM using jetPRIME® (Polyplus) according to the manufacturer's protocol. To achieve optimal knockdown efficiency, two rounds of silencing were performed. For transient overexpression of proteins in HEK293T cells, 6 µg plasmid DNA per 10 cm dish were transfected using calcium phosphate as described in[59]. Primary astrocytes (~2 weeks in culture) were transfected using lipofectamin 2000 (Invitrogen) with either 50 nM siRNA (for silencing experiments) or at a 1:2 ratio of DNA to lipofectamin in Opti-MEM as described in the manufacturer's instructions. Astrocytes were processed ~48 h post transfection.

**Cell lines**

HeLa, HEK293T, Cos7 and A431 cells were obtained from ATCC. Sum159pt cells were a gift from the Cancer Biology Department (IIBM, Madrid). U-2 OS cells were provided by Claus Scheidereit (MDC, Berlin). Sum159pt cells were cultured in HAM F-12 (Lonza) with 5% heat-inactivated fetal bovine serum (FBS) (Gibco), 10 mM HEPES, 1 µg/ml hydrocortisone and 5µg/m insulin. All other cell lines were cultured in DMEM with 4.5 g/L glucose (Lonza) containing 10% heat-inactivated FBS, 100 U/ml penicillin, and 100 µg/ml streptomycin (Gibco). Cells were routinely tested for and devoid of mycoplasma contamination.

**Preparation and culture of primary astrocytes from conditional AP-2µ KO mice and induced AP-2µ deletion**

The generation and genotyping of conditional AP-2µ KO mice (*Mus musculus*, C57BL/6J) is described in[26]. The AP-2 lox/lox animals were crossed with a tamoxifen-inducible Cre line (B6.Cg-Tg(CAG-cre/Esr1*)5Amc/J; The Jackson Laboratory).

Primary astrocytes were prepared from neonatal mice (P0-P3) essentially as previously described[60]. Cultured astrocytes were identified by their positive glial fibrillary acidic protein (GFAP) staining. To deplete AP-2µ, cultured astrocytes from floxed conditional AP-2µ KO mice expressing a tamoxifen-inducible Cre recombinase were treated with 0.1 µM (Z)-4-hydroxytamoxifen (Sigma) the day after plating. Astrocytes derived from floxed littermates that were Cre negative were used as controls and treated with equal amounts of (Z)-4-hydroxytamoxifen.

**RNA isolation and relative quantitative real-time PCR**

RNA was isolated using the quick-start protocol of RNease Mini Kit (Quiagen) following the manufacturer's protocol. Quantification of RNA yields was done with a multi-mode microplate

reader (SPECTROstar® Nano from BMG Labtech). A reverse transcription kit (SuperScript IV; Invitrogen) was used to reverse transcribe RNA (200-500 ng) in a 20-µl reaction using oligo(dT) and random hexamer primers. Quantitative real-time PCR was performed in a StepOnePlus™ Real-Time PCR System (Thermofisher) with 20 µl reaction volume containing 5 µl of cDNA, 1 µl gene expression assay (TaqMan) and 10 µl gene expression master mix (TaqMan). Thermocycler parameters were: 50°C for 2 min and 95°C for 10 min, followed by 40 cycles of 95°C for 15 s and 60°C for 1 min. The results were analyzed by the comparative threshold cycle (Ct) method and normalized to GAPDH as an internal control, and the values are expressed as fold change compared to WT untreated astrocytes. TaqMan probes used for qPCR are listed in Supplementary Table 4.

**Immunocytochemistry and confocal imaging**

HeLa, HEK293T, Cos7, A431, Sum159pt, U-2 OS and primary cells seeded on coverslips were fixed for 13 min with 4% paraformaldehyde (w/v, PFA) in phosphate-buffered saline (PBS) solution on ice and washed three times with PBS. Cells were permeabilized and blocked in blocking solution (PBS, 10% goat serum and 0.3% Triton X-100) for 30 min and incubated with primary antibodies diluted in blocking solution for 1 h. After three washes with PBS coverslips were incubated for 1 h with secondary antibodies diluted in blocking solution, followed by three washes in PBS. Alternatively, for LC3 and LAMP2 immunostaining, cells were fixed for 30 min with 4% PFA (w/v) in PBS at room temperature and permeabilized with digitonin (200 µg/ml) for 15 min. Coverslips were mounted in Immu-Mount (Thermo Fisher) with 1.5 mg/ml DAPI (Sigma) to stain nuclei and were visualized routinely using the Zeiss laser scanning confocal microscope LSM710.

**Labeling lysosomes with Lysotracker**

To stain lysosomes, astrocytes were incubated with 250-500 nM of Lysotracker Red™ or Green™ in 1 ml of complete fresh medium for 45 min, washed 3 times, and imaged immediately in live-cell imaging solution (HBSS containing 5% FCS and 20 mM HEPES pH 7.4) using a Zeiss laser scanning confocal microscope LSM710.

**Determination of cathepsin activity**

Cathepsin L/B activity was monitored by the Magic Red Cathepsin detection kit (BioRad). Astrocytes were loaded with Magic Red Cathepsin L/B reagent in complete fresh DMEM for 60 min at 37°C in the dark, washed 3 times and imaged immediately in live-cell imaging solution

(HBSS containing 5% FCS and 20mM HEPES pH 7.4) using the Zeiss laser scanning confocal microscope LSM710. Pretreatment with chloroquine (0.1 mM, 2 h) was done to inhibit cathepsin activity.

**Image analysis**

Quantitative analysis of fluorescence intensity was performed in ImageJ. Cells were selected as ROIs, and a minimum of 20 cells per sample were analyzed to determine the average fluorescence intensity per cell. For LC3 puncta determination, a threshold was set to extract the punctate signal from cytosolic background, and puncta were analyzed using the 'Analyze particles' ImageJ module to determine the number of fluorescent puncta considering those from 0.2 to 1.5 μm diameter.

**Evaluation of protein aggregation**

The detection of total aggregated protein was measured by the ProteoStat® Protein Aggregation Assay (Enzo Lifesciences, NZ) following the manufacturer's protocol. Samples were visualized using a Zeiss laser scanning confocal microscope LSM710. Quantitative analysis was performed in ImageJ. Cells were selected as ROIs and segmentation via intensity based on thresholding, and the 'Analyze particles' module were used to quantify the number of aggregates. For astrocytes transfected with GFP-α–synuclein A53T, GFP positive cells were selected as ROIs, nuclei were excluded, the Gaussian Blur filter was applied, and the "Maximum detection" module was used to quantify the number of objects.

**Electron microscopy**

For routine electron microscopy preparation, astrocytes were grown in 6 cm dishes, fixed with 2% glutaraldehyde in PBS, pelleted and incubated with 1% osmium tetroxide and 1.5% potassium hexacyanoferrat (III), dehydrated in methanol and embedded into Epoxy resin. After polymerization, 60 nm sections were collected, contrasted and imaged with transmission electron microscopy. Morphometric analyzes were performed by superimposing a grid over the montage image covering the astrocytic profile. Grid intersections targeting cytoplasm and organelles of interest were counted, and the volume fraction of organelles was determined.

**Lysosomal $Ca^{2+}$ measurements**

Lysosomal $Ca^{2+}$ was evaluated on the basis of an Oregon Green 488 BAPTA-5N and tetramethylrhodamine 10 kD-conjugated dextran fluorescence assay. Primary astrocytes from

WT and AP-2μ KO mice were loaded overnight with 5 μM Oregon Green 488 BAPTA-5N (a pH-insensitive $Ca^{2+}$ indicator) and 0.5 mg/ml tetramethylrhodamine 10 kD-conjugated dextran ($Ca^{2+}$ insensitive). Astrocytes were washed, and the indicators were chased for 2 h to allow lysosomal accumulation of dyes post-endocytosis. The fluorescence intensity of Oregon Green 488 BAPTA-5N is indicative of the luminal $Ca^{2+}$ concentration in lysosomes. Imaging was performed in cell imaging buffer (Hank's balanced salt solution (HBSS) containing 5% FCS, 10 mM HEPES) using a Nikon Eclipse Ti microscope, equipped with a x40 oil-immersion objective, a sCMOS camera (Neo, Andor), a 200 W mercury lamp (Lumen 200, Prior) and operated by open-source ImageJ-based Micro-Manager software. Regions of interest (ROI) were defined as areas above a defined fluorescence threshold in the acquired images at 488 nm excitation. The mean intensity ratio between 488 nm and 568 nm excitation was calculated for each ROI. For each genotype, at least 10 different cells from 3 independent litters with at least 10 single lysosomes each were analyzed.

**Cytosolic pH and pH recovery measurements**

The fluorescent pH-sensitive indicator BCECF-AM was used to detect intracellular pH (pHi) in individual cells. Primary astrocytes from WT and AP-2μ KO mice were loaded with 5 μM BCECF-AM for 30 min at 37°C in complete fresh DMEM. After washing twice with HEPES buffer (140 mM NaCl, 5.36 mM KCl, 0.81 mM $MgSO_4$, 1.27 mM $CaCl_2$, 0.44 mM $KH_2PO_4$, 0.33 mM $Na_2HPO_4$, 5.55 mM glucose, 20 mM HEPES, pH 7.4) fluorescence was recorded at 440 and 490 nm excitation and 530 nm emission for 40 cycles at 15 s intervals. Images were acquired while alternating between 2 fluorescence filter cubes (OG1: excitation filter BP 436/20, dichroic FT 455, emission filter 540/50; OG2: excitation filter BP 480/40, dichroic FT 510, emission filter 540/50) using a Nikon Eclipse Ti microscope, equipped with a ×40 oil-immersion objective, a sCMOS camera (Neo, Andor), a 200 W mercury lamp (Lumen 200, Prior) and operated by open-source ImageJ-based Micro-Manager software. To measure NHE activity an acid challenge was performed by the $NH_4Cl$-prepulse technique. Intracellular fluorescence ratios were determined for 40 cycles at 15 s intervals. Cells were bathed in HEPES buffer during the first four cycles, exposed to 20 mM $NH_4Cl$ added to the HEPES buffer with an equi-osmolar reduction in the NaCl concentration during the next eight cycles, and again incubated in HEPES buffer during the last 28 cycles. Recovery of pHi (ΔpHi) during the last 28 cycles is calculated by subtracting the pHi after 2 min (eight cycles) exposure to $NH_4Cl$ from the pHi measured every min during the recovery for a total of 7 min, and NHE activity was determined as $\Delta pHi/\Delta t$. The fluorescence ratio (490/440 nm) was determined and calibrated to indicated $pH_i$ by

interpolation between the measured fluorescence ratios after 20 min of exposure to one of 3 calibration buffers (130 mM KCl; 1 mM $MgCl_2$; 15 mM HEPES; 15 mM MES) with a pH of either 6.3, 6.9 or 7.5 and containing 56 µM nigericin and 10 µM of monensin, ionophores that allow to equilibrate intracellular pH with extracellular pH. The mean ratio values were plotted as a function of pH to create the calibration curve.

**$Ca^{2+}$ and $Na^+$ imaging**

Measurements of cytosolic $Ca^{2+}$ were performed at 20°C in HBSS buffer (137 mM NaCl, 5.4 mM KCl, 0.5 mM $MgSO_4$, 0.4 mM $MgCl_2$, 1.26 mM $CaCl_2$, 0.64 $KH_2PO_4$, 3 mM $NaHCO_3$, 5.5 mM Glucose, 20 mM HEPES pH 7.4). Primary astrocytes from WT and AP-2µ KO mice were loaded with 2 µM Fluo-4/AM or Fluo-8/AM together with 0.02% pluronic for 30 min at 37°C in complete fresh DMEM medium. Prior to imaging, astrocytes were washed 3 times in imaging buffer, and fluorescence was recorded in 0.5 ml of HBSS buffer at 480 nm excitation and 530 nm emission with three 20 s kinetic cycles using the Zeiss laser scanning confocal microscope LSM710 (pinhole at maximum and very low laser power). For $Na^+$ imaging primary astrocytes from WT and AP-2µ KO mice were loaded with 12 µM ANG-2 (Abcam) for 40 min at 37°C in loading buffer (135 mM NaCl, 5.4 mM KCl, 20 mM HEPES, 1.3 mM $CaCl_2$, 0.8 mM $MgSO_4$, 9.78 mM $NaH_2PO_4$, 20 mM glucose, pH 7.4) and 0.02% pluronic. After washing 3 times with imaging buffer (160 mM NaCl, 5.4 mM KCl, 20 mM HEPES, 1.3 mM $CaCl_2$, 0.8 mM $MgSO_4$, 9.78 mM $NaH_2PO_4$, 20 mM glucose, pH 7.4) astrocytes were recorded in 0.5 ml of imaging buffer at 480 nm excitation and 530 nm emission with three 20 s kinetic cycles using a Zeiss laser scanning confocal microscope LSM710 (pinhole at maximum and very low laser power). For in situ calibration, calibration solutions containing different $Na^+$ concentrations as well as ionophores (3 µM gramicidin D, 10 µM monensin) to equilibrate extra- and intracellular sodium concentrations (from 0 to 140 mM and using $Na^+$-gluconate to have proper osmolarity) were used. After correction for background fluorescence, fluorescence intensity was analyzed. At least 5 small ROIs per cell were selected and a minimum of 50 cells per sample were evaluated for each experiment.

**Manipulations of extracellular $Na^+$**

Astrocytes seeded on coverslips were washed with PBS and incubated with physiological Ringer´s solution (155 mM NaCl, 5 mM KCl, 2 mM $CaCl_2$, 1 mM $MgCl_2$, 2 mM $NaH_2PO_4$, 10 mM HEPES, 10 mM glucose, 0.5 mg/ml BSA, pH 7,4) or low $Na^+$ Ringer´s solution (30 mM NaCl, 125 mM CholineCl, 5 mM KCl, 2 mM $CaCl_2$, 1 mM $MgCl_2$, 2 mM $NaH_2PO_4$, 10 mM

HEPES, 10 mM glucose, 0.5 mg/ml BSA, pH 7,4) for 15 h. Cells were then processed for immunocytochemistry or for $Ca^{2+}$ imaging.

**Treatments**

For blocking endocytosis, astrocytes or HeLa cells were treated with Dynasore (80 μM), Pitstop 2 (30 μM), Wortmannin (500 nM), GDC0941 (50 nM), CK666 (50 μM), Cytochalasin D (100 nM) or methyl-β-cyclodextrin (MβDC; 50 μM) for the indicated times before the experiments were performed. For manipulations of cytosolic $Ca^{2+}$, astrocytes were treated for 15 h with DMSO or thapsigargin (500 nM), the cell-permeant $Ca^{2+}$ chelator BAPTA-AM (10 μM), or EGTA (2 mM).

The calcineurin inhibitor Cyclosporin A (10 μM) was applied to the cells during 15 h before the experiments were performed. For manipulations of cytosolic $Na^{+}$, astrocytes were treated for 15 h with DMSO or Ouabain (50 μM) to increase intracellular $Na^{+}$. To reduce cytosolic $Na^{+}$, astrocytes were incubated for 15 h extracellularly with 155 mM or 30 mM $Na^{+}$. For inducing hyperosmotic stress, astrocytes were treated with D-mannitol at concentrations from 0 to 300 mOsm (final osmolarity of 600 mOsm) for the indicated times.

**Transferrin uptake**

Astrocytes seeded on coverslips were serum-starved overnight and treated with 50 μg/ml Tf-Alexa488/647 for 20 min at 37°C. Cells were washed twice with ice-cold PBS and then acid-washed at pH 5.3 (0.1 M Na-acetate, 0.2 M NaCl) for 1 min on ice. The coverslips were washed twice with ice-cold PBS and fixed with 4% PFA for 30 min at room temperature. Cells were washed three times with PBS, followed by immunocytochemistry staining as described in the Immunocytochemistry section. Transferrin uptake was analyzed using a Nikon Eclipse Ti microscope, equipped with a ×40 oil-immersion objective, a sCMOS camera (Neo, Andor), a 200 W mercury lamp (Lumen 200, Prior) and operated by open-source ImageJ-based Micro-Manager software.

**Preparation of lysates and immunoblot-based analysis**

Cultured cells were washed briefly with PBS and scraped into lysis buffer (20 mM HEPES pH 7.4, 100 mM KCl, 2 mM $MgCl_2$, 2 mM PMSF, 1% Triton X-100, 0.6% protease inhibitor cocktail (Sigma)). Lysates were incubated on a rotating wheel at 4°C for 30 min, followed by centrifugation at 17,000g for 10 min at 4°C. The protein concentration of the supernatant was determined by the Bradford or BCA assay. Protein samples (between 15 and 40 μg) were

adjusted to 1× Laemmli sample buffer, resolved by sodium dodecyl sulfate polyacrylamide gel electrophoresis (SDS/PAGE) and processed for immunoblotting. Bound primary antibodies were detected by incubation with IRDye 680/800CW-conjugated secondary antibodies via the Odyssey Fc Imaging system (LI-COR Biosciences). Alternatively, HRP-conjugated secondary antibodies and ECL substrate (LI-COR; P/N 926–80100) were used. Chemiluminescence was detected with the Bio-Rad ChemiDoc MP Imaging System. Protein intensities were normalized to a loading control (actin, Hsc70 or GAPDH as indicated). All experiments were performed at least two times. Uncropped immunoblots are provided in the Source Data files for each figure.

**Surface biotinylation**

HEK293T cells or astrocytes were placed on ice, washed twice with ice-cold $PBS^{2+}$ (137 mM NaCl, 2.7 mM KCl, 8.1 mM $Na_2HPO_4$, 0.5 mM $CaCl_2$, 1 mM $MgCl_2$, pH 7.4) and incubated with 0.5 mg/ml Sulfo-NHS-LC-Biotin (EZ-Link, Pierce/Thermo Scientific) in $PBS^{2+}$ while shaking for 30 min at 4°C. The biotinylation solution was removed, and surplus biotin was quenched by two 5 min washes with 50 mM glycine in $PBS^{2+}$ at 4°C on a shaker. Cells were harvested, and lysates were prepared as described above. Biotinylated molecules were isolated by a 1.5 h incubation of lysates with streptavidin beads on a rotating wheel at 4°C. After centrifugation at 3,500 *g* the supernatant was transferred to a fresh tube. Beads were washed extensively, and bound protein was eluted with Laemmli buffer by heating to 65°C for 15 min, separated by SDS–PAGE and analyzed by immunoblotting. N-Cadherin and actin were used as markers for the membrane and cytosol fraction, respectively. All experiments were performed at least 2 times.

**Nuclear fractionation**

To obtain nuclear and cytoplasmic fractions, astrocytes were rinsed with cold PBS, scraped in subcellular fractionation buffer (20 mM HEPES, 10 mM KCl, 2 mM $MgCl_2$, 1 mM EDTA, and 1 mM dithiothreitol plus protease inhibitor cocktail) and centrifuged for 5 min at 3000 rpm at 4º C. The supernatants were used as cytoplasmic fractions. The pellet was then washed with subcellular fractionation buffer, homogenized with a 25-gauge needle 20 times and centrifuged again at 3000 rpm for 10 min at 4º C. The supernatants were discarded, and the pellets were resuspended in TBS with 0.1 % SDS, sonicated and used as nuclear fractions. Protein concentrations from each sample were measured in duplicate by Bradford method, and equal amounts of proteins were loaded into each well and subjected to SDS-PAGE. All experiments were performed at least 2 times. Nucleoporin p62 (NUP62) and Histone 1x were

used as markers for the nuclear fraction, while GAPDH was used as a marker for the cytosolic fraction.

**Purification of GST-fusion proteins and affinity-chromatography assays**

GST fusion proteins were expressed in *E. coli* BL21 (DE3) and purified according to the manufacturer's instructions. Affinity chromatography was performed using 75 µg of recombinant GST, GST-AP-2µ WT, GST-AP-2µ Yxxø-motif binding-defective mutant (GST-AP-2µ (D176A,W421A)) and GST-AP-2ασ hemicomplex and 1 mg cell lysate from NHE7-EGFP expressing HEK293T prepared as detailed above. After 2 h on a rotating wheel at 4ºC and following extensive washes, bound proteins were eluted by adding 40 µl of 1x Laemmli sample buffer and boiling for 5 min at 95°C. After a brief centrifugation, the supernatant was transferred to a new tube and samples were analyzed by SDS-PAGE and immunoblotting.

**Mass spectrometry-based quantification of surface protein accumulation**

Astrocytes were cultured for 20 days in L-lysine- and L-arginine-free DMEM/10% FCS (Thermo Fisher Scientific Inc.) supplemented either with the 'heavy' amino acids 13C6-L-lysine and 13C6,15N4-L-arginine (Silantes GmbH) in case of AP-2µ KO astrocytes or normal 'light' amino acids in case of WT. For surface biotinylation, cells were treated as described above. After protein determination, WT and AP-2µ KO lysates were brought to the same concentration and mixed 1:1. Biotinylated molecules were isolated as described previously. For liquid chromatography (LC)–mass spectrometry (MS)/MS analysis, Coomassie-stained lanes were cut into slices, and proteins were digested with trypsin as described[61]. Mass spectra were acquired in a data-dependent mode with one MS survey scan (with a resolution of 30,000) in the Orbitrap and MS/MS scans of the four most intense precursor ions in the LTQ. Identification and quantification of proteins were carried out with version 1.2.0.18 of the MaxQuant software package as described[62]. Data were searched against an international protein index (IPI) mouse protein database (version 3.68).

**Statistics and Reproducibility**

Values are depicted as mean ± SEM or mean ± SD as indicated in the figure legends. For comparisons between two experimental groups statistical significance of normally distributed data was analyzed by two-sample, two-sided unpaired or paired Student's t-tests (see figure legends). For comparisons between more than two experimental groups statistical significance of normally distributed data was analyzed by one-way ANOVA with post-hoc test such as the

Tukey post-hoc test (see figure legends). One-sample two-sided t-tests were used for comparisons with control group values that had been set to 1 for normalization purposes and that therefore did not fulfill the requirement of two-sample t-tests or one-way ANOVA concerning the homogeneity of variances. The Benjamini-Hochberg procedure was used to correct for multiple testing based on the acceptance of a false discovery rate of 5% (see figure legends). GraphPad Prism version 8 software was used for statistical analysis. The level of significance is indicated in the figures by asterisks (*=$p \leq 0.05$; **=$p \leq 0.01$; ***=$p \leq 0.001$; ****=$p \leq 0.0001$) and provided in the figure legends as exact p-value as obtained by the indicated statistic test. No statistical method was used to pre-determine sample size as sample sizes were not chosen based on pre-specified effect size. Instead, multiple independent experiments were carried out using several sample replicates as detailed in the figure legends. Cortical astrocytes from several newborn mice of identical genotype from the same litter were pooled and analyzed. Cortical astrocytes were randomly allocated to experimental groups i.e. to different treatments (drugs, transfection with plasmids etc.). Whenever possible, data were evaluated in a blinded manner.

# Figure 1

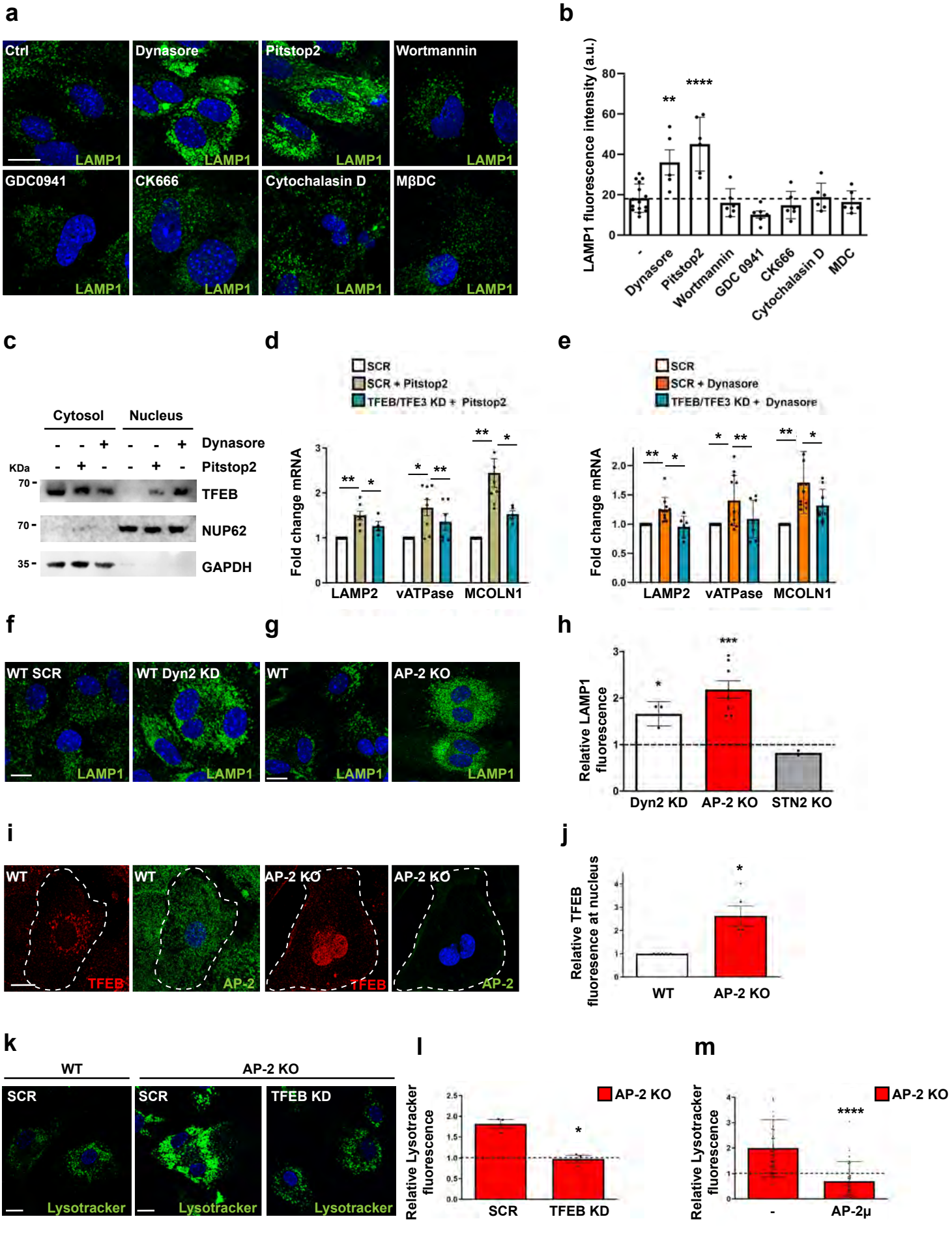
a
Ctrl
Dynasore
Pitstop2
Wortmannin
GDC0941
CK666
Cytochalasin D
MβDC
LAMP1
b
LAMP1 fluorescence intensity (a.u.)
-
Dynasore
Pitstop2
Wortmannin
GDC 0941
CK666
Cytochalasin D
MDC
c
Cytosol
Nucleus
Dynasore
Pitstop2
KDa
70
TFEB
NUP62
GAPDH
35
d
SCR
SCR + Pitstop2
TFEB/TFE3 KD + Pitstop2
Fold change mRNA
LAMP2
vATPase
MCOLN1
e
SCR
SCR + Dynasore
TFEB/TFE3 KD + Dynasore
f
WT SCR
WT Dyn2 KD
g
WT
AP-2 KO
h
Relative LAMP1 fluorescence
Dyn2 KD
AP-2 KO
STN2 KO
i
TFEB
AP-2
j
Relative TFEB fluoresence at nucleus
k
SCR
TFEB KD
Lysotracker
l
Relative Lysotracker fluorescence
m
AP-2µ

# Figure 2

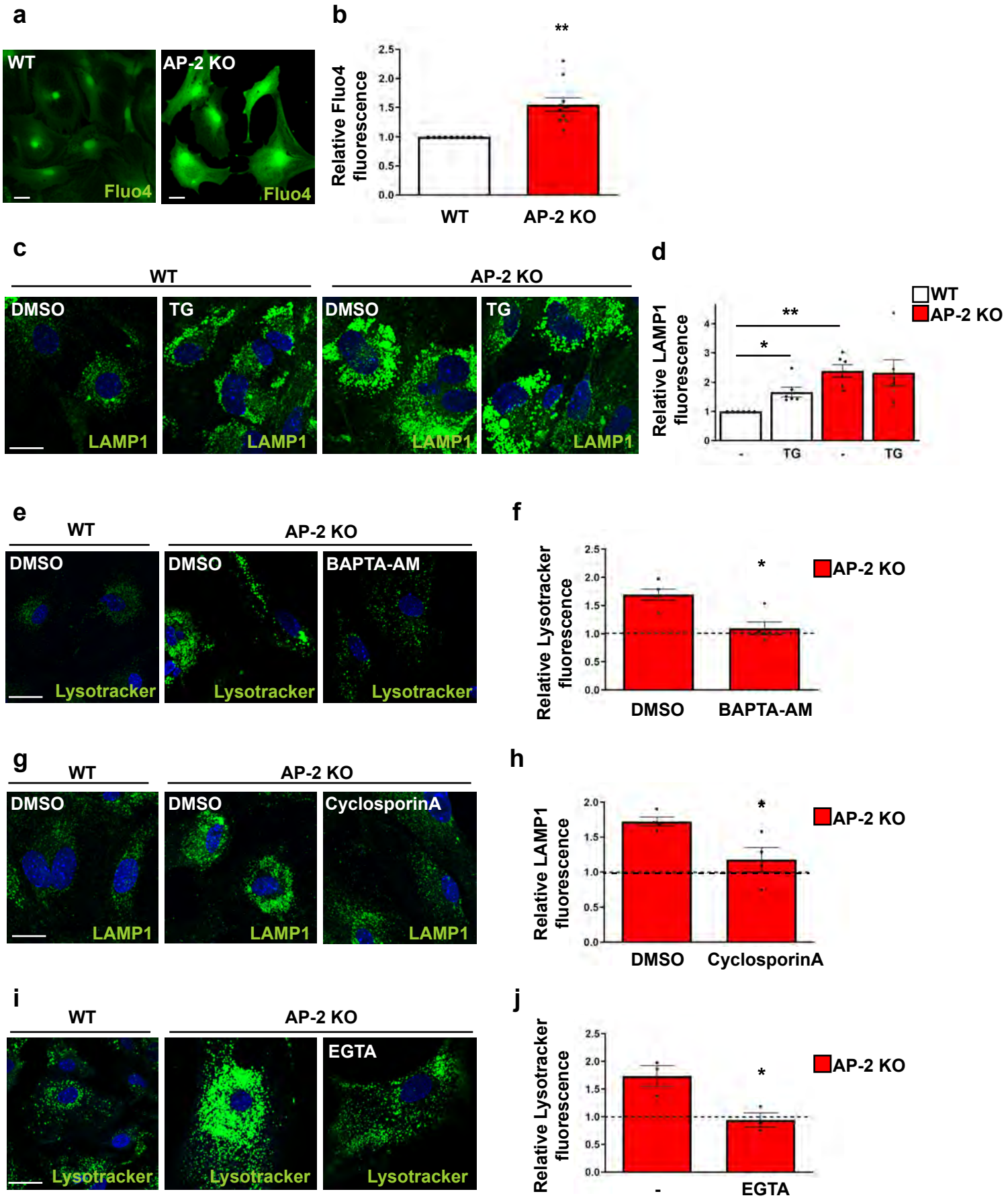
a
WT
Fluo4
AP-2 KO
Fluo4
b
Relative Fluo4 fluorescence
2.5
2.0
1.5
1.0
0.5
0.0
**
WT
AP-2 KO
c
WT
AP-2 KO
DMSO
LAMP1
TG
LAMP1
DMSO
LAMP1
TG
LAMP1
d
WT
AP-2 KO
Relative LAMP1 fluorescence
4
3
2
1
0
**
*
-
TG
-
TG
e
WT
AP-2 KO
DMSO
Lysotracker
DMSO
Lysotracker
BAPTA-AM
Lysotracker
f
AP-2 KO
Relative Lysotracker fluorescence
2.5
2.0
1.5
1.0
0.5
0.0
*
DMSO
BAPTA-AM
g
WT
AP-2 KO
DMSO
LAMP1
DMSO
LAMP1
CyclosporinA
LAMP1
h
AP-2 KO
Relative LAMP1 fluorescence
2.0
1.5
1.0
0.5
0.0
*
DMSO
CyclosporinA
i
WT
AP-2 KO
Lysotracker
Lysotracker
EGTA
Lysotracker
j
AP-2 KO
Relative Lysotracker fluorescence
2.5
2.0
1.5
1.0
0.5
0.0
*
-
EGTA

# Figure 3

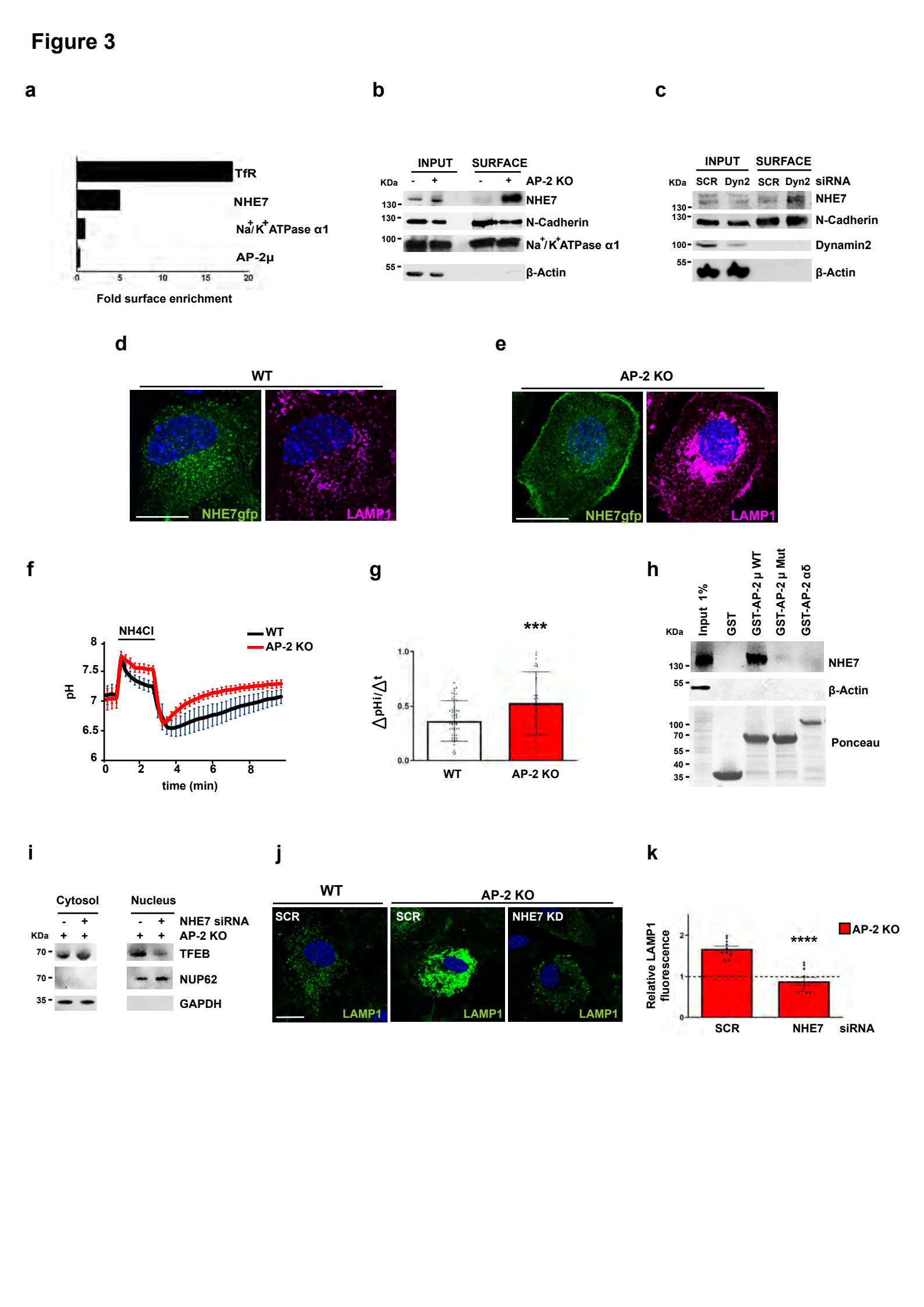
a
TfR
NHE7
Na+/K+ATPase α1
AP-2μ
0
5
10
15
20
Fold surface enrichment
b
INPUT
SURFACE
KDa
- + - +
AP-2 KO
130
NHE7
130
N-Cadherin
100
Na+/K+ATPase α1
55
β-Actin
c
INPUT
SURFACE
KDa
SCR Dyn2 SCR Dyn2
siRNA
130
NHE7
130
N-Cadherin
100
Dynamin2
55
β-Actin
d
WT
NHE7gfp
LAMP1
e
AP-2 KO
NHE7gfp
LAMP1
f
NH4Cl
WT
AP-2 KO
pH
8
7.5
7
6.5
6
0
2
4
6
8
time (min)
g
***
ΔpHi/Δt
1.0
0.5
0.0
WT
AP-2 KO
h
KDa
Input 1%
GST
GST-AP-2 μ WT
GST-AP-2 μ Mut
GST-AP-2 αδ
130
NHE7
55
β-Actin
100
70
55
40
35
Ponceau
i
Cytosol
Nucleus
- + - +
KDa + + + +
NHE7 siRNA
AP-2 KO
70
TFEB
70
NUP62
35
GAPDH
j
WT
AP-2 KO
SCR
LAMP1
SCR
LAMP1
NHE7 KD
LAMP1
k
AP-2 KO
Relative LAMP1 fluorescence
2
1
0
****
SCR
NHE7
siRNA

# Figure 4

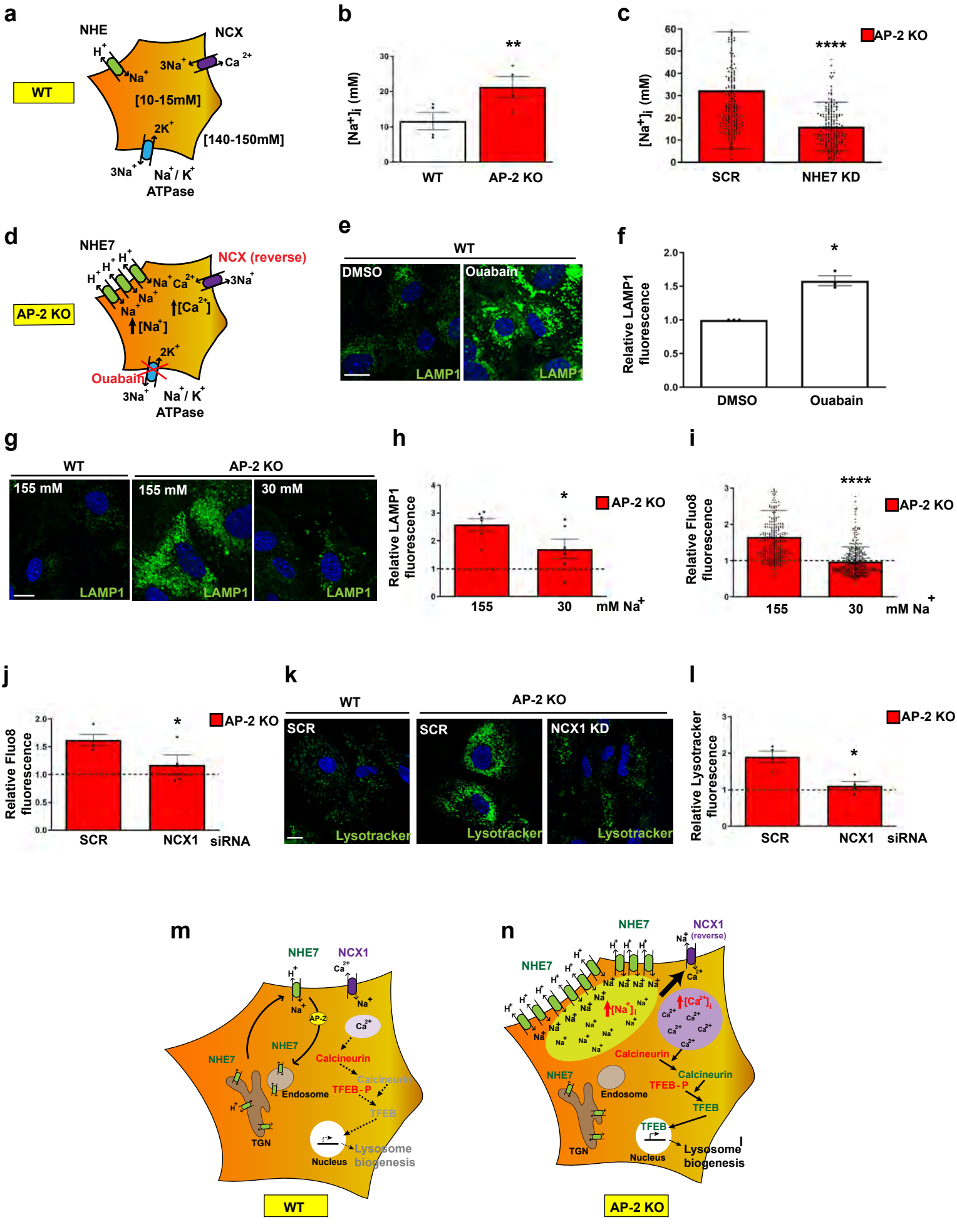
a
NHE
NCX
WT
[10-15mM]
[140-150mM]
Na+ / K+ ATPase
b
[Na+]i (mM)
WT
AP-2 KO
c
AP-2 KO
[Na+]i (mM)
SCR
NHE7 KD
d
NHE7
NCX (reverse)
AP-2 KO
Ouabain
Na+ / K+ ATPase
e
WT
DMSO
Ouabain
LAMP1
f
Relative LAMP1 fluorescence
DMSO
Ouabain
g
WT
AP-2 KO
155 mM
30 mM
LAMP1
h
Relative LAMP1 fluorescence
AP-2 KO
155
30
mM Na+
i
Relative Fluo8 fluorescence
AP-2 KO
155
30
mM Na+
j
Relative Fluo8 fluorescence
AP-2 KO
SCR
NCX1 siRNA
k
WT
AP-2 KO
SCR
NCX1 KD
Lysotracker
l
Relative Lysotracker fluorescence
AP-2 KO
SCR
NCX1 siRNA
m
NHE7
NCX1
AP-2
Calcineurin
TFEB-P
TFEB
Endosome
TGN
Nucleus
Lysosome biogenesis
WT
n
NHE7
NCX1 (reverse)
[Na+]i
[Ca2+]i
Calcineurin
TFEB-P
TFEB
Endosome
TGN
Nucleus
Lysosome biogenesis
AP-2 KO

# Figure 5

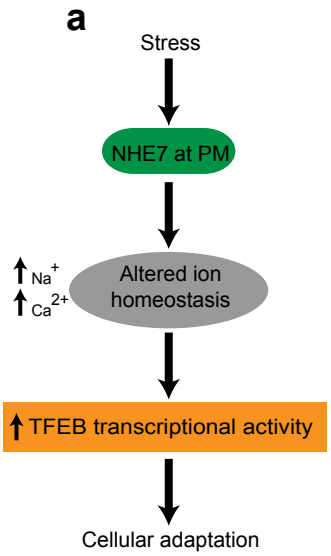
a
Stress
NHE7 at PM
Na+
Ca2+
Altered ion homeostasis
TFEB transcriptional activity
Cellular adaptation

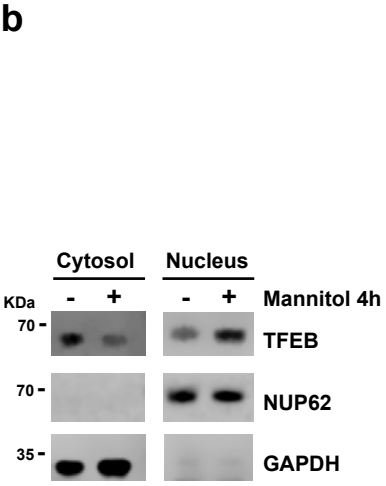
b
Cytosol
Nucleus
KDa
- + - +
Mannitol 4h
70
TFEB
70
NUP62
35
GAPDH

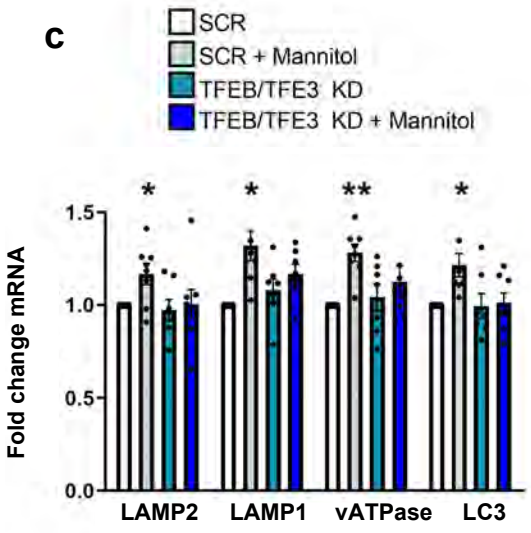
c
SCR
SCR + Mannitol
TFEB/TFE3 KD
TFEB/TFE3 KD + Mannitol
Fold change mRNA
1.5
1.0
0.5
0.0
LAMP2
LAMP1
vATPase
LC3

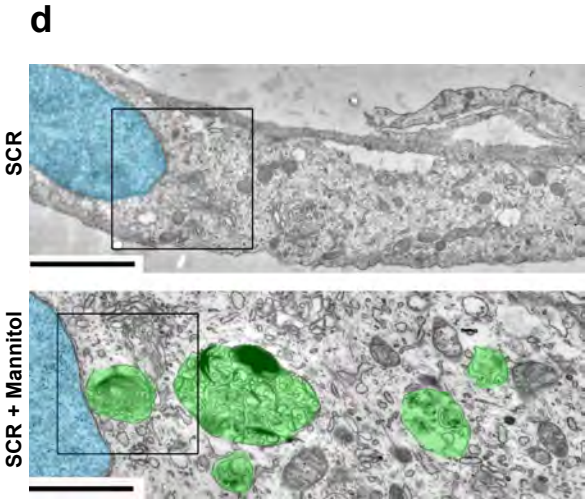
d
SCR
SCR + Mannitol

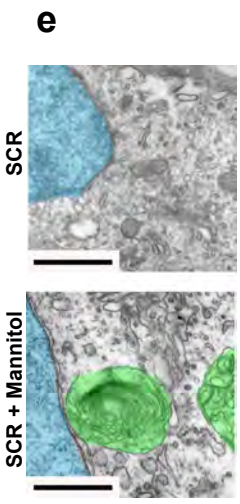
e
SCR
SCR + Mannitol

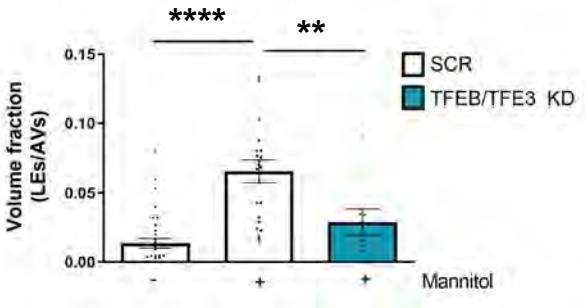
f
****
**
SCR
TFEB/TFE3 KD
Volume fraction (LEs/AVs)
0.15
0.10
0.05
0.00
Mannitol

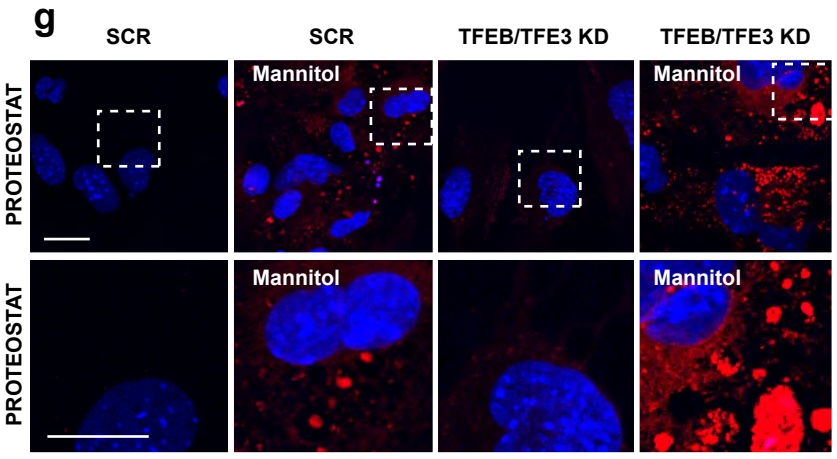
g
SCR
SCR
TFEB/TFE3 KD
TFEB/TFE3 KD
PROTEOSTAT
Mannitol
PROTEOSTAT
Mannitol

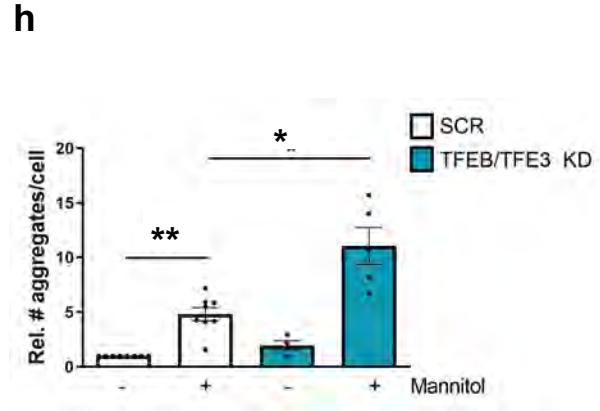
h
SCR
TFEB/TFE3 KD
*
**
Rel. # aggregates/cell
20
15
10
5
0
Mannitol

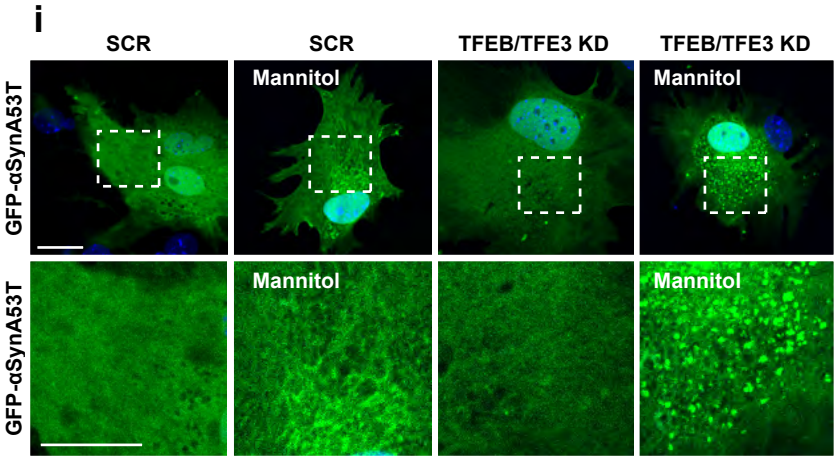
i
SCR
SCR
TFEB/TFE3 KD
TFEB/TFE3 KD
GFP-αSynA53T
Mannitol
GFP-αSynA53T
Mannitol

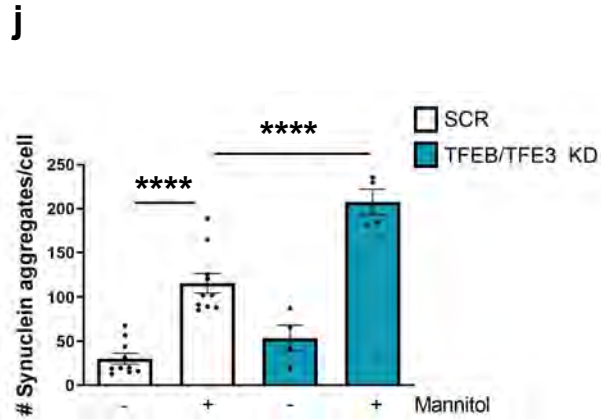
j
SCR
TFEB/TFE3 KD
****
****
# Synuclein aggregates/cell
250
200
150
100
50
0
Mannitol

# Figure 6

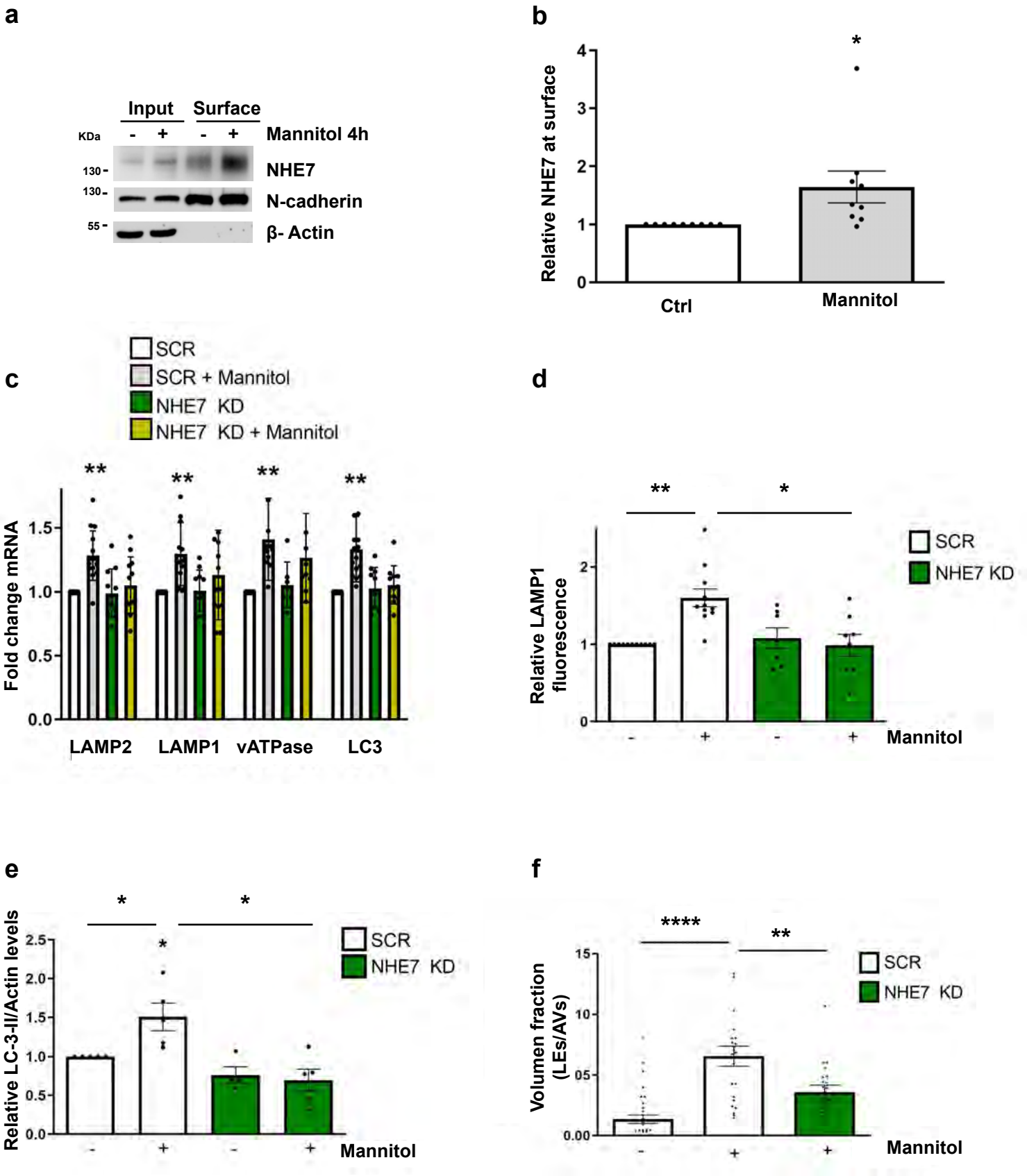
a
Input
Surface
KDa
- + - +
Mannitol 4h
130-
NHE7
130-
N-cadherin
55-
β- Actin
b
Relative NHE7 at surface
4
3
2
1
0
*
Ctrl
Mannitol
c
SCR
SCR + Mannitol
NHE7 KD
NHE7 KD + Mannitol
Fold change mRNA
1.5
1.0
0.5
0.0
**
**
**
**
LAMP2
LAMP1
vATPase
LC3
d
Relative LAMP1 fluorescence
2
1
0
**
*
SCR
NHE7 KD
- + - +
Mannitol
e
Relative LC-3-II/Actin levels
2.5
2.0
1.5
1.0
0.5
0.0
*
*
*
SCR
NHE7 KD
- + - +
Mannitol
f
Volumen fraction (LEs/AVs)
15
10
05
0.00
****
**
SCR
NHE7 KD
- + +
Mannitol

# Figure 7

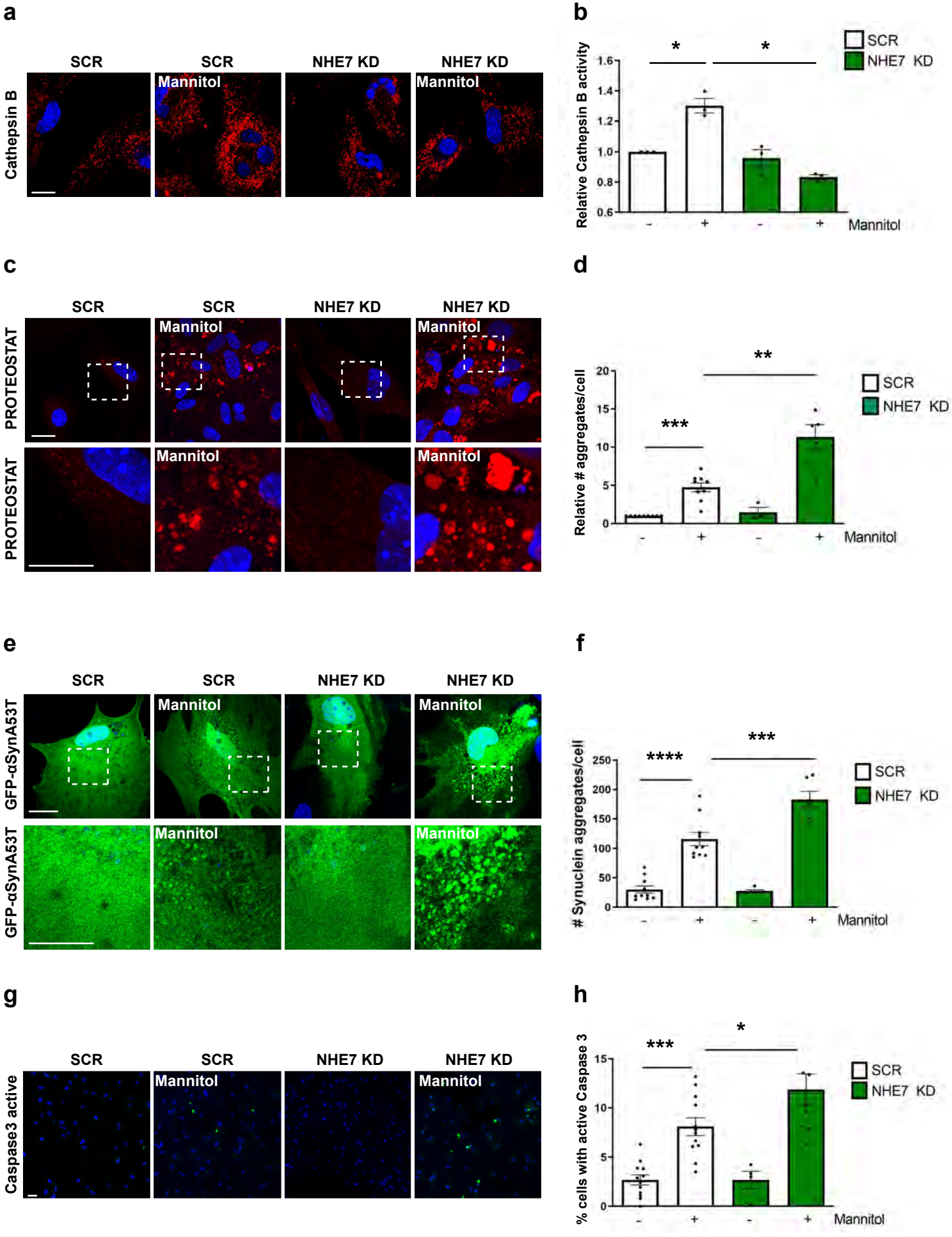
a
SCR
SCR
NHE7 KD
NHE7 KD
Cathepsin B
Mannitol
Mannitol
b
Relative Cathepsin B activity
1.6
1.4
1.2
1.0
0.8
0.6
*
*
SCR
NHE7 KD
-
+
-
+
Mannitol
c
SCR
SCR
NHE7 KD
NHE7 KD
PROTEOSTAT
PROTEOSTAT
Mannitol
Mannitol
Mannitol
Mannitol
d
Relative # aggregates/cell
20
15
10
5
0
**
***
SCR
NHE7 KD
-
+
-
+
Mannitol
e
SCR
SCR
NHE7 KD
NHE7 KD
GFP-αSynA53T
GFP-αSynA53T
Mannitol
Mannitol
Mannitol
Mannitol
f
# Synuclein aggregates/cell
250
200
150
100
50
0
****
***
SCR
NHE7 KD
-
+
-
+
Mannitol
g
SCR
SCR
NHE7 KD
NHE7 KD
Caspase3 active
Mannitol
Mannitol
h
% cells with active Caspase 3
15
10
5
0
***
*
SCR
NHE7 KD
-
+
-
+
Mannitol

**Extended Data Fig. 1**

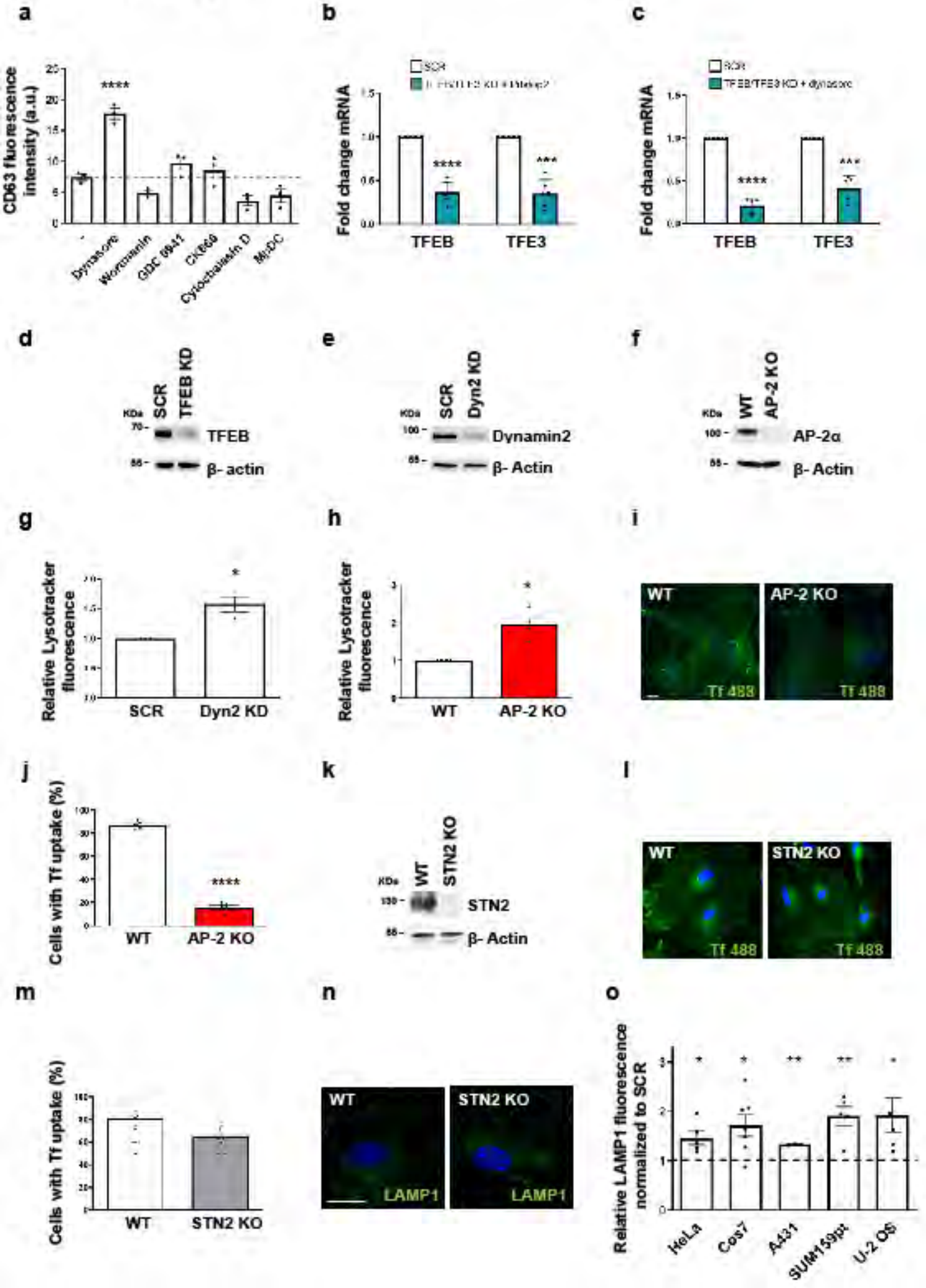

**Extended Data Fig. 2**

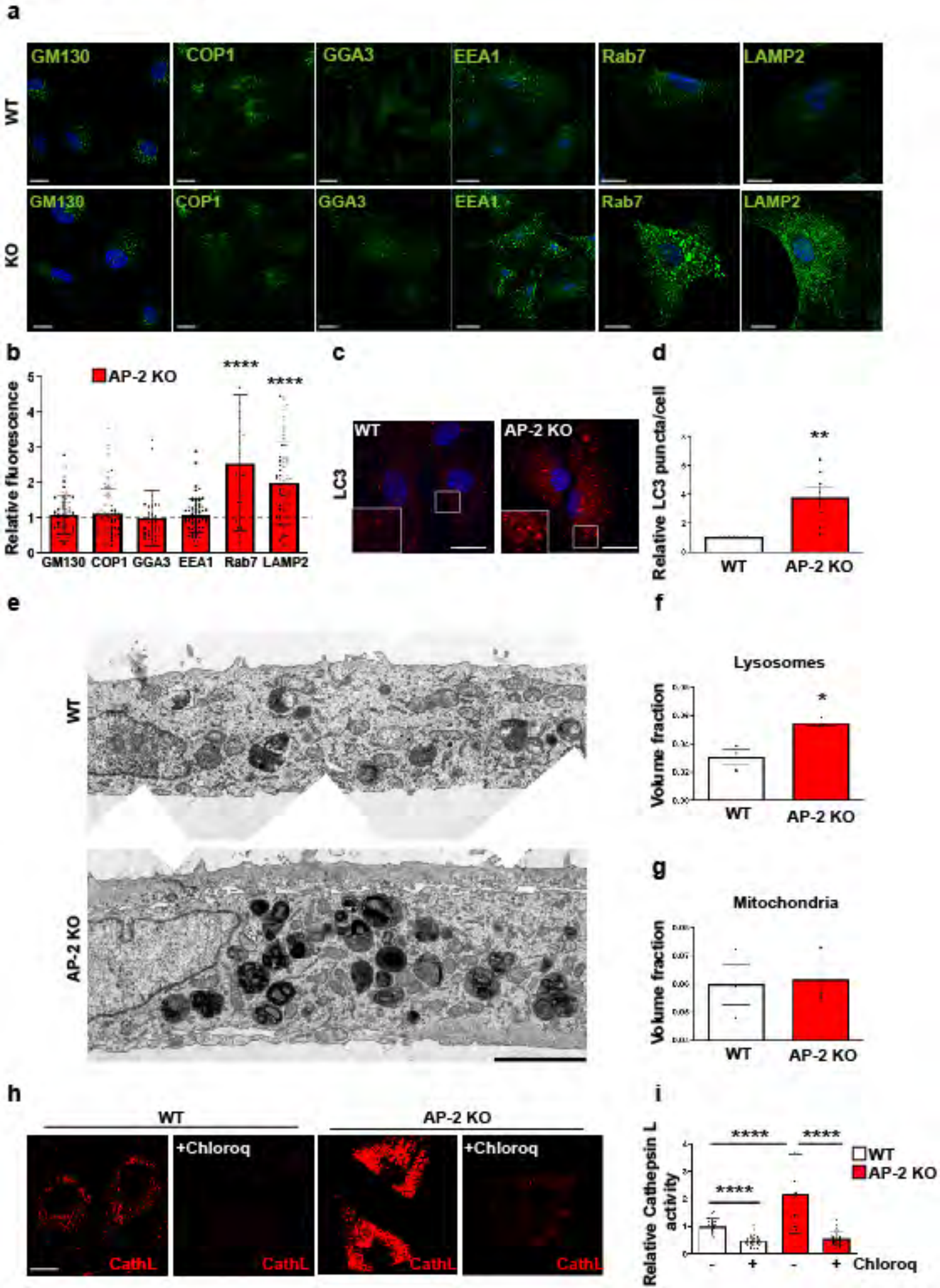

# Extended Data Fig. 3

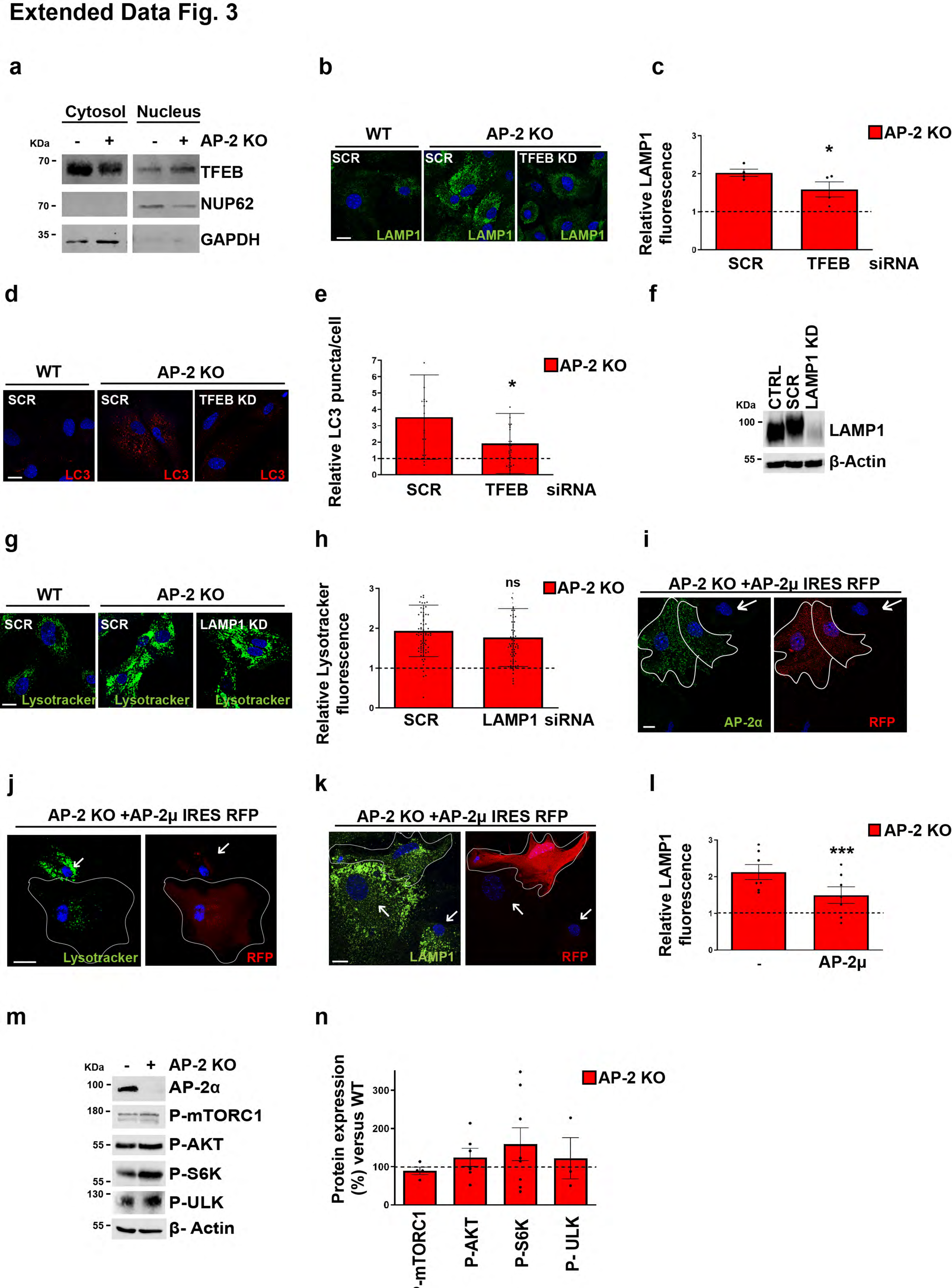

# Extended Data Fig. 4

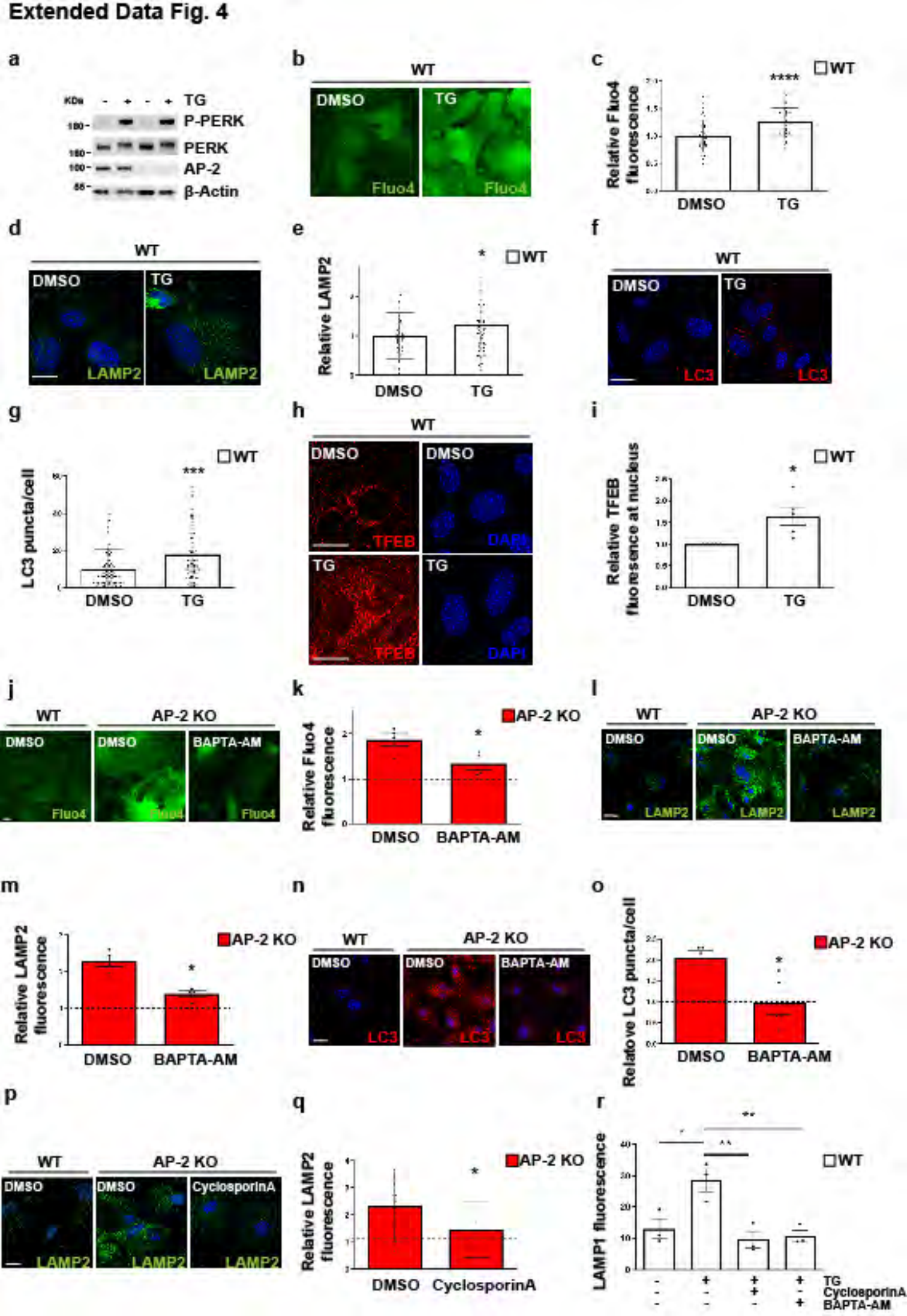

# Extended Data Fig. 5

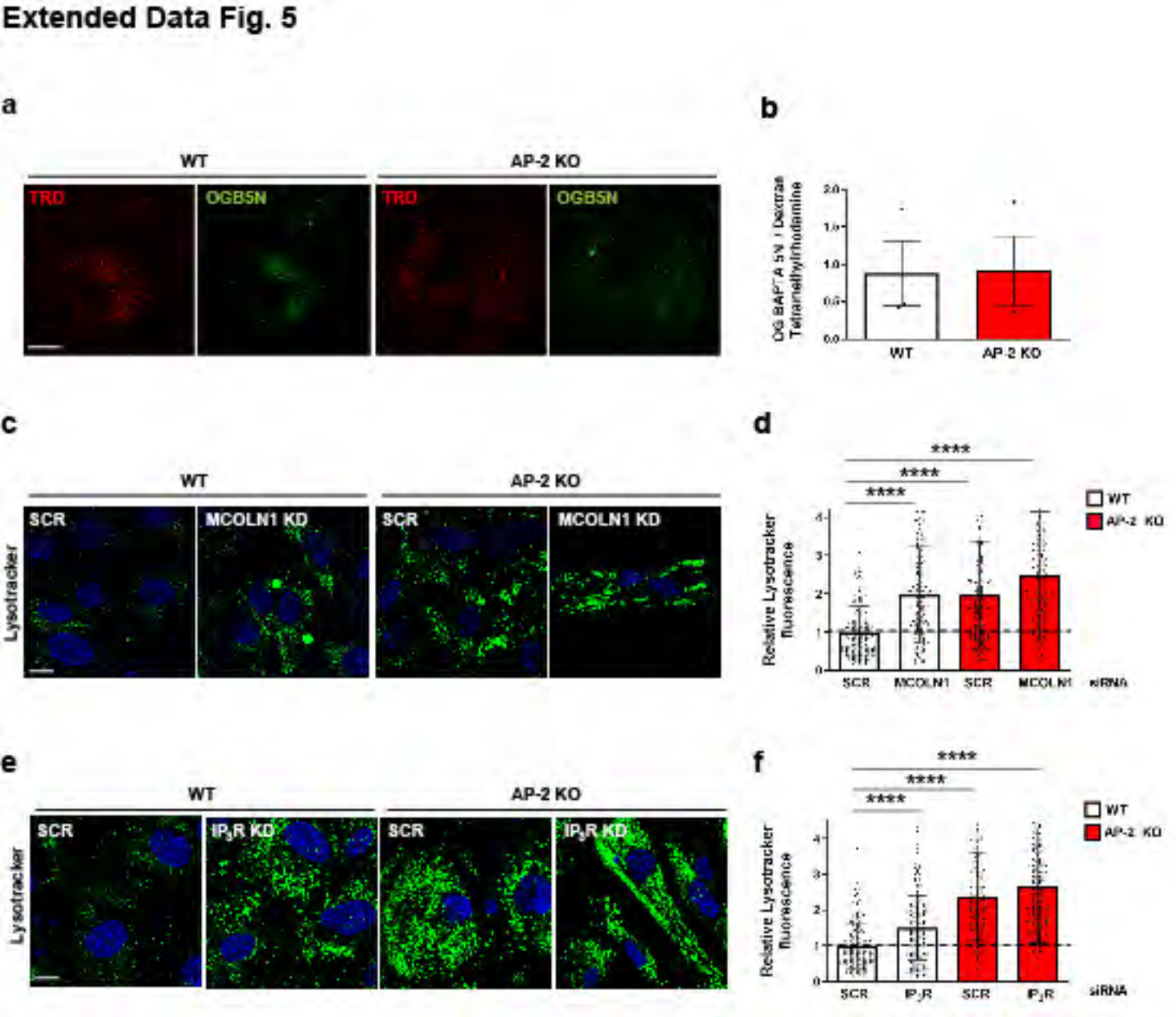

# Extended Data Fig. 6

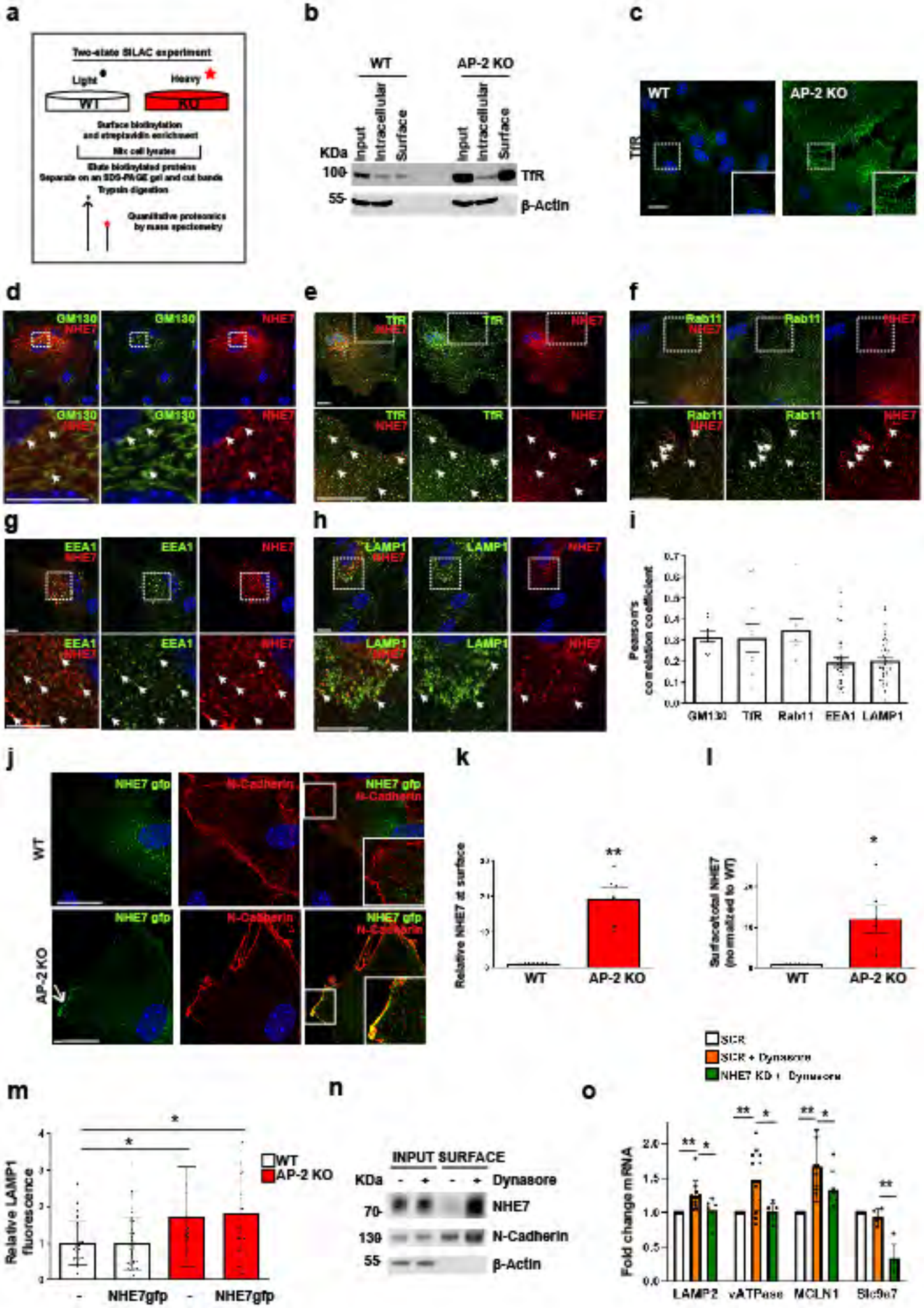

# Extended Data Fig. 7

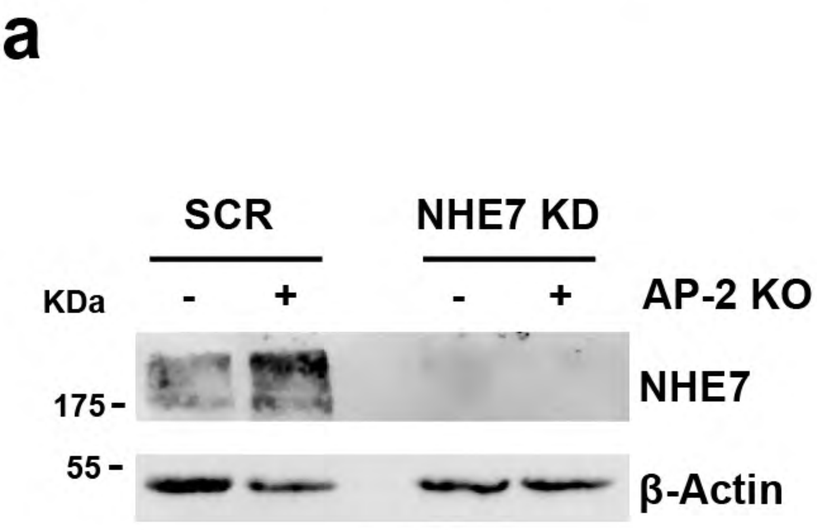


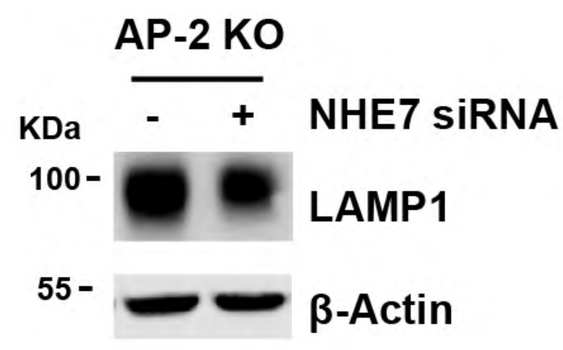


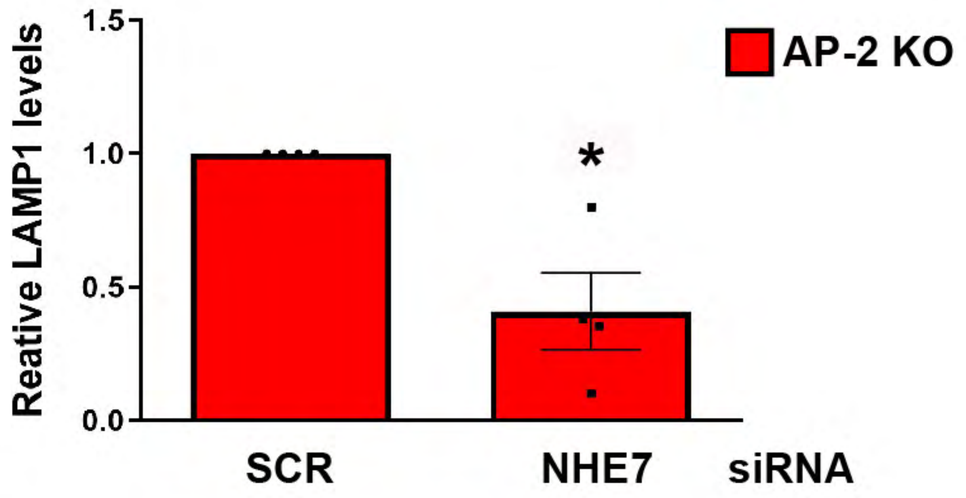


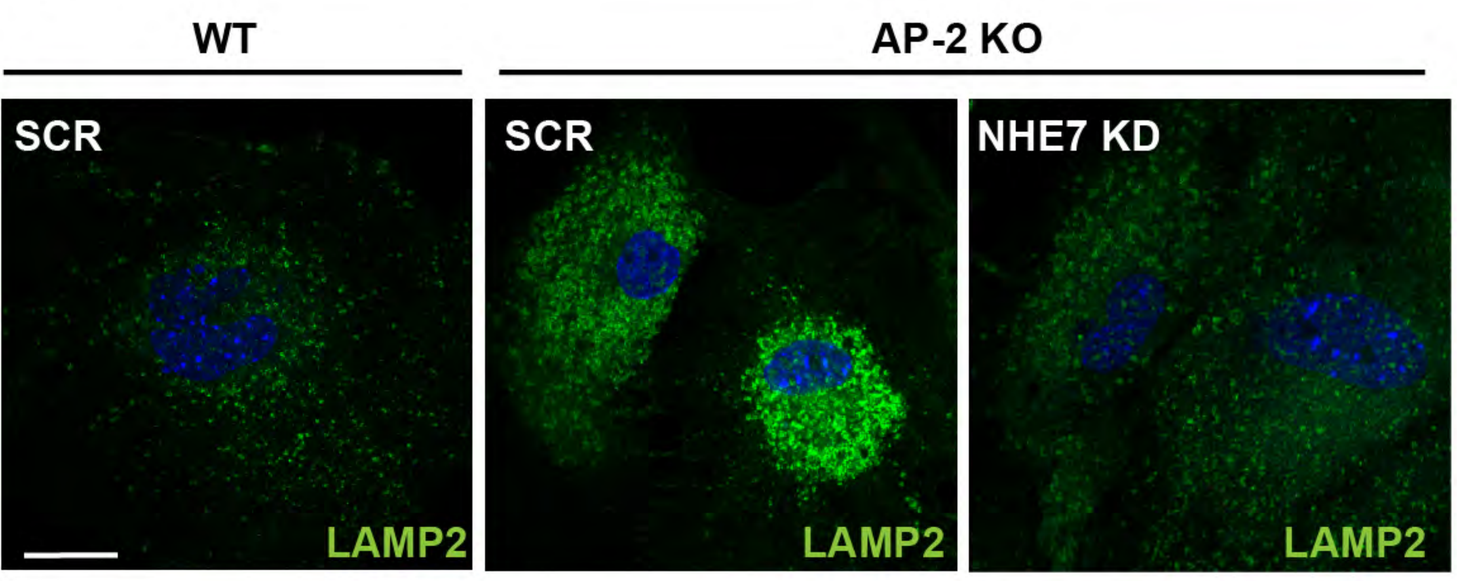


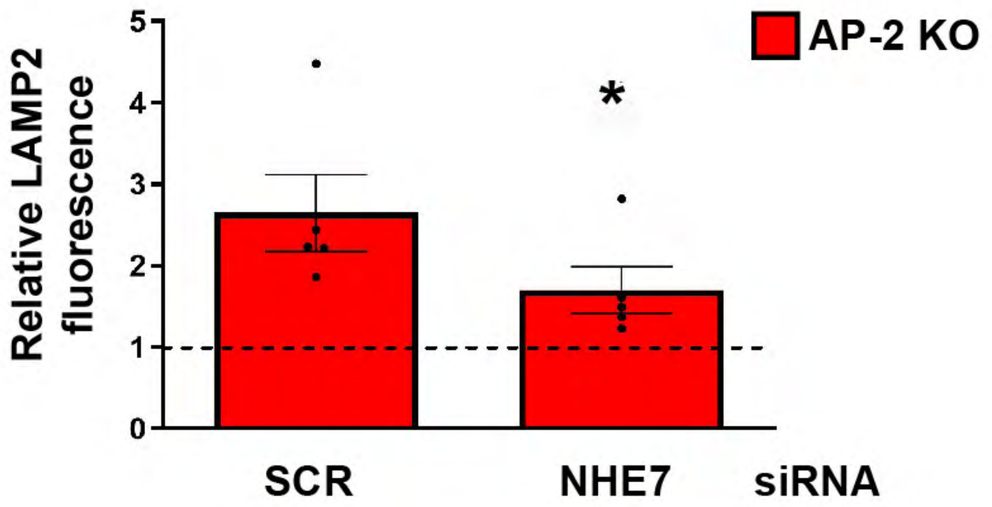


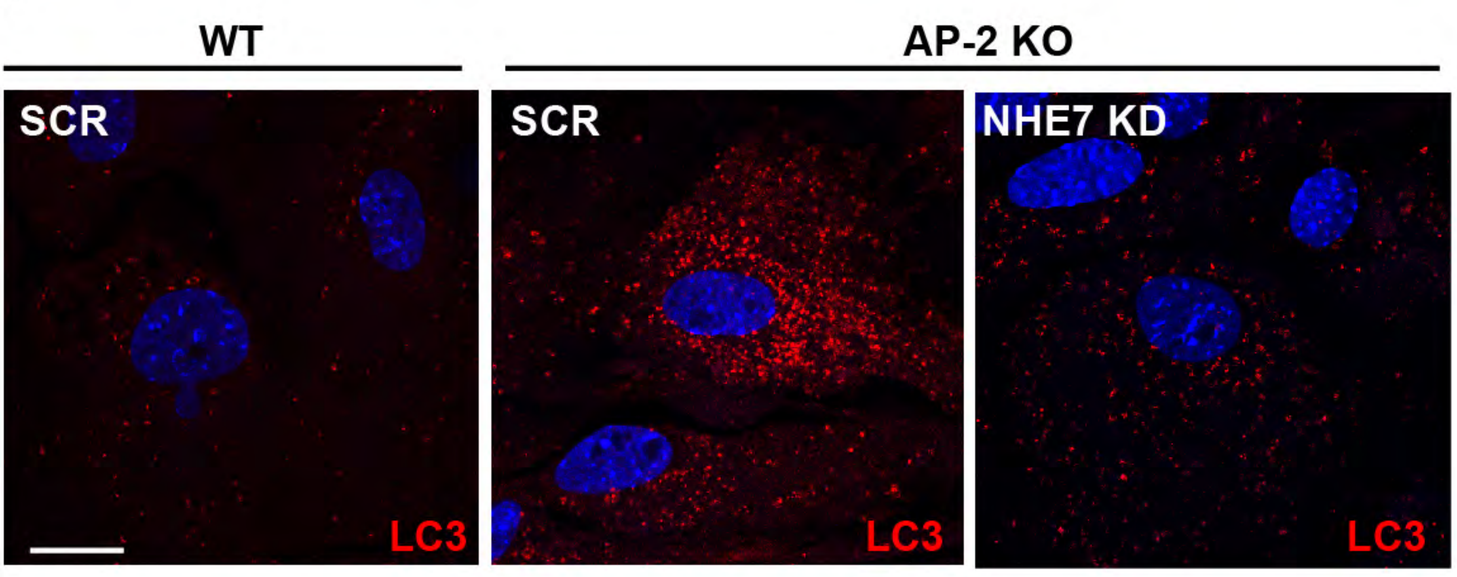


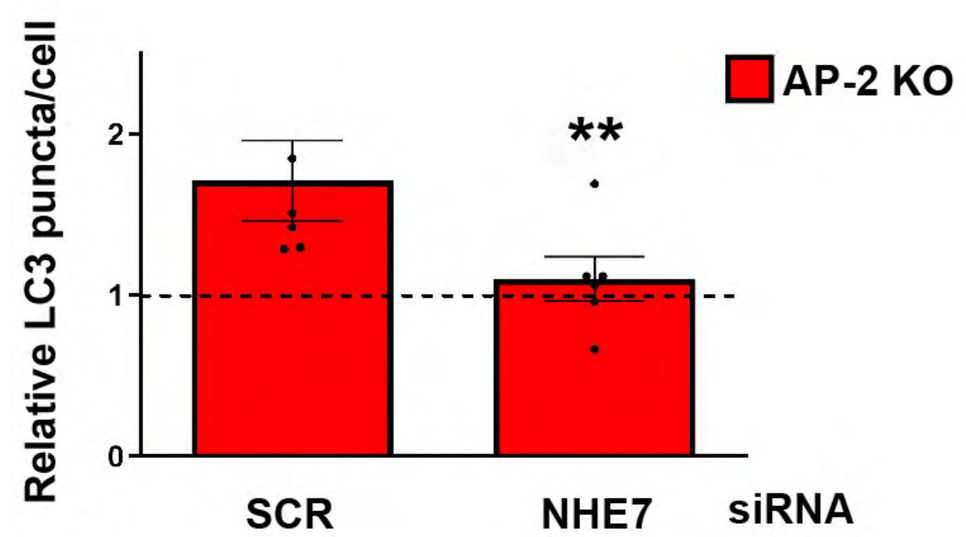


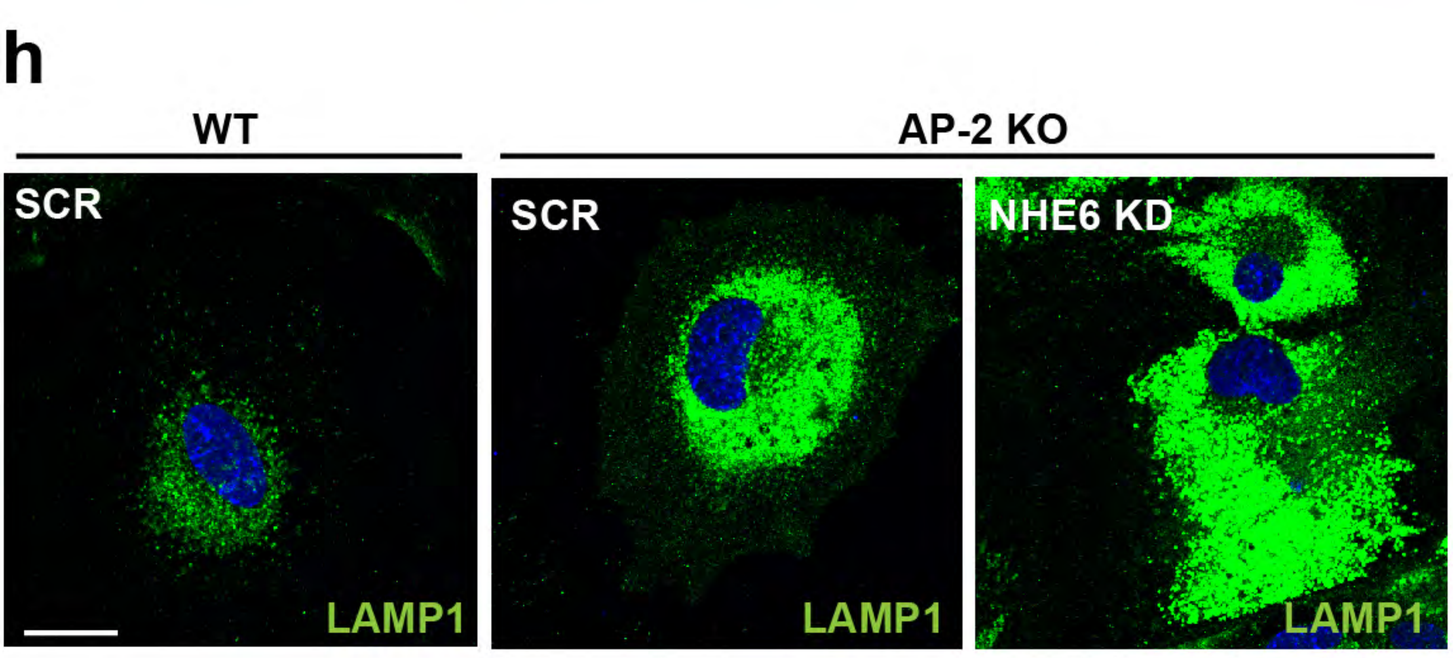


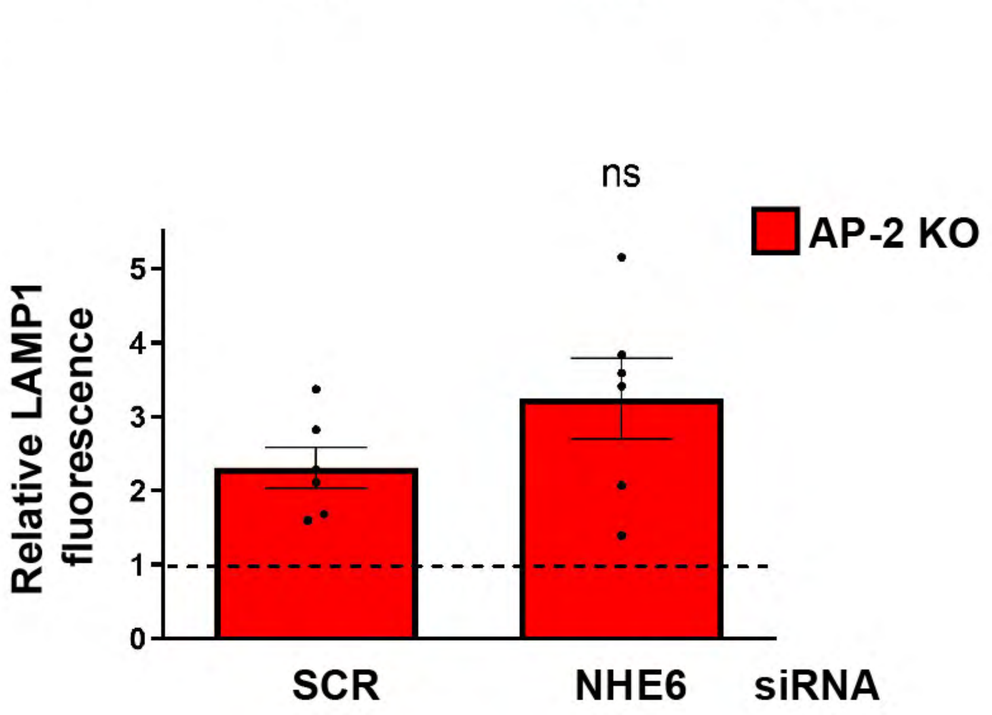


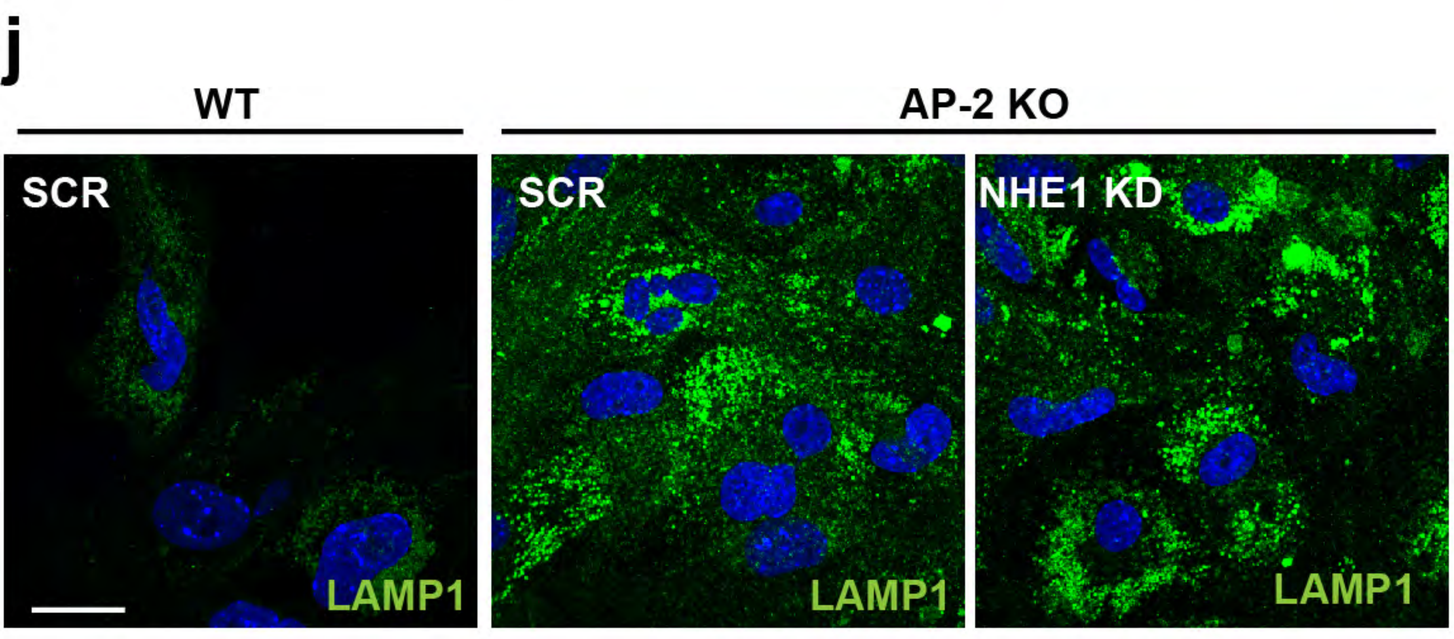


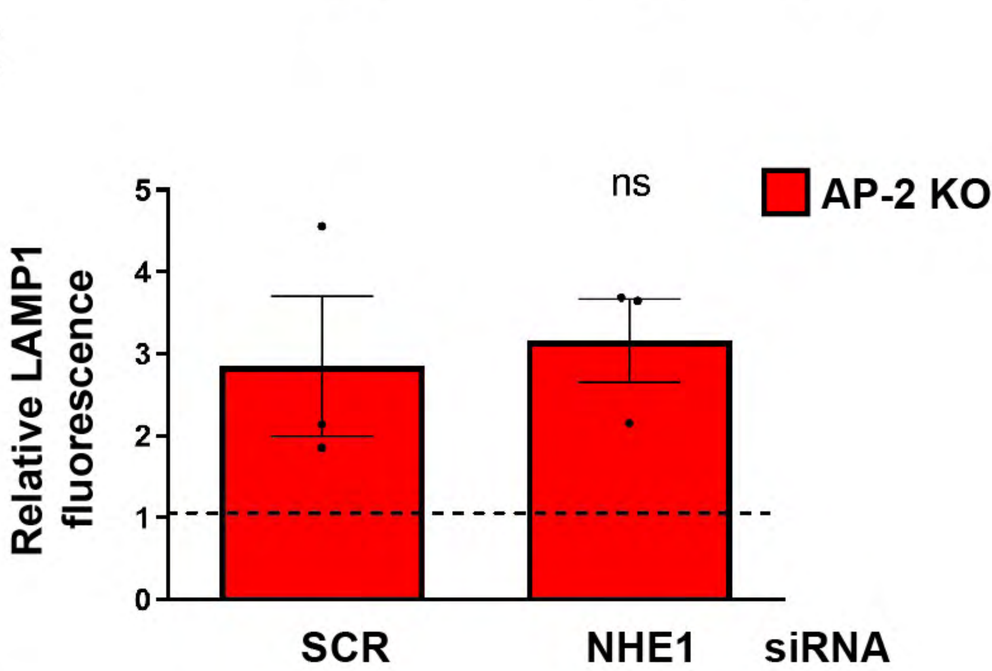


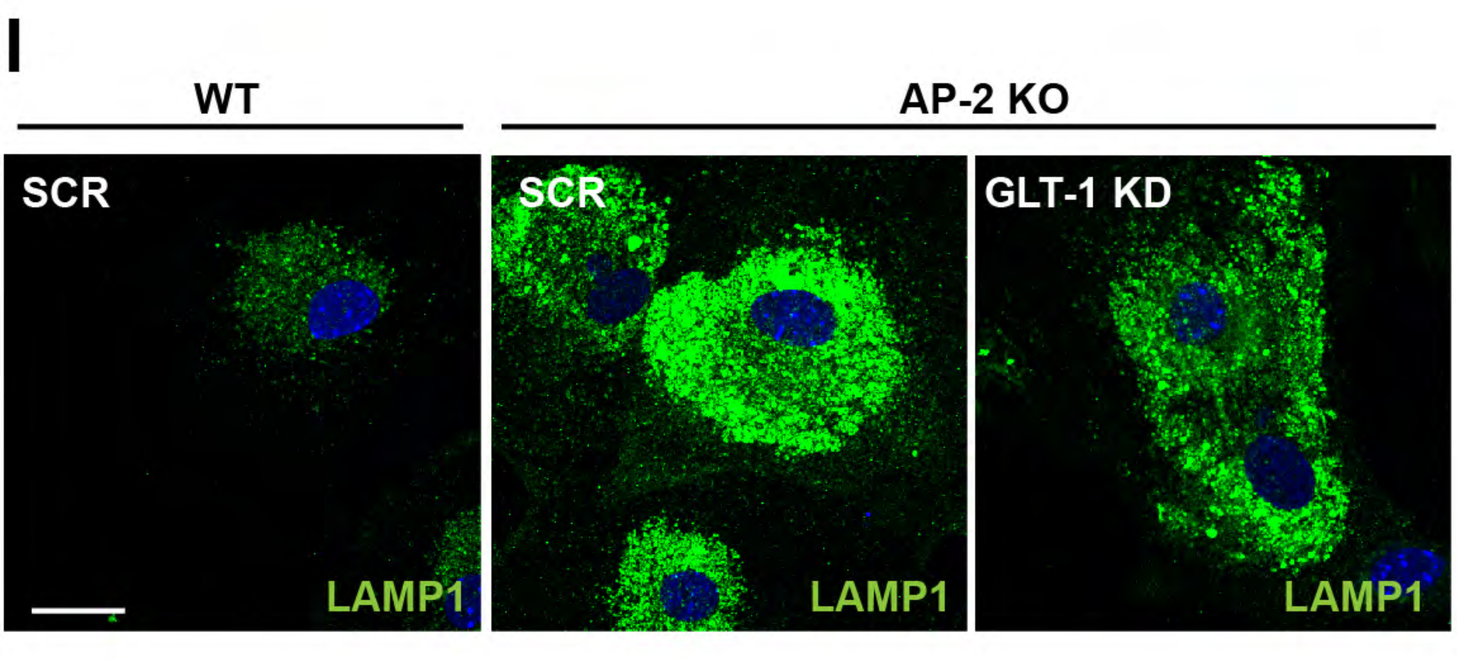


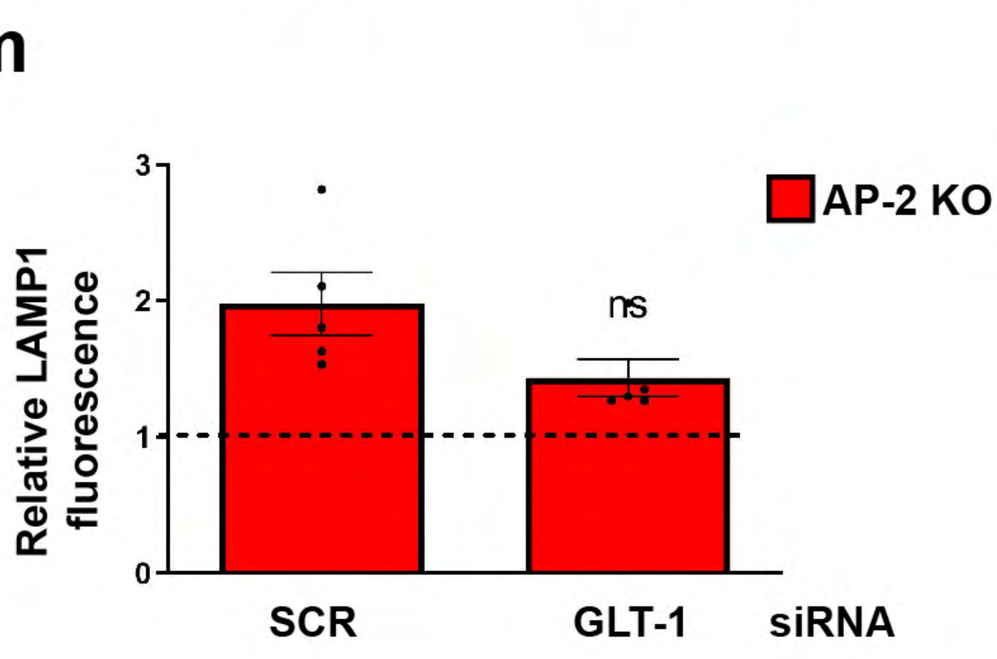

# Extended Data Fig. 8

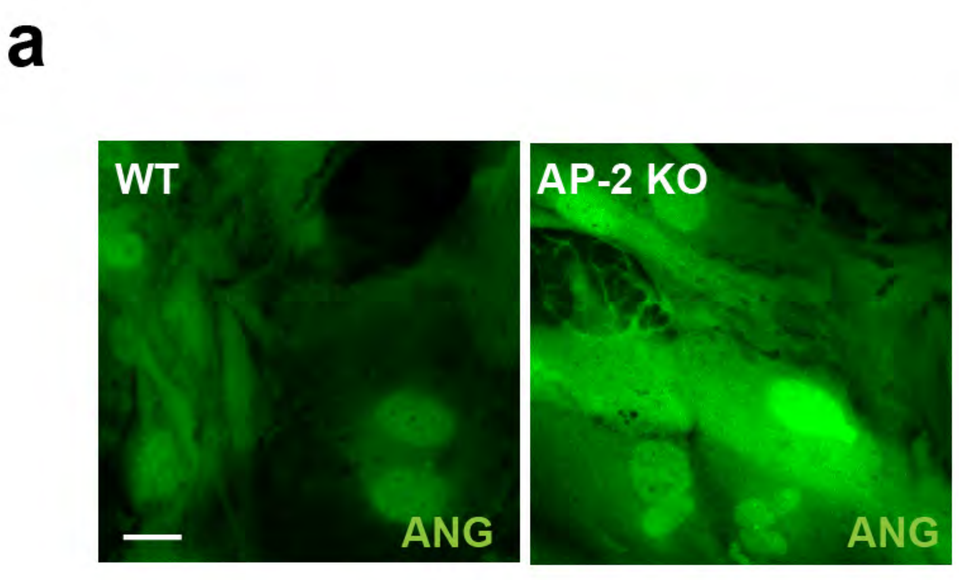


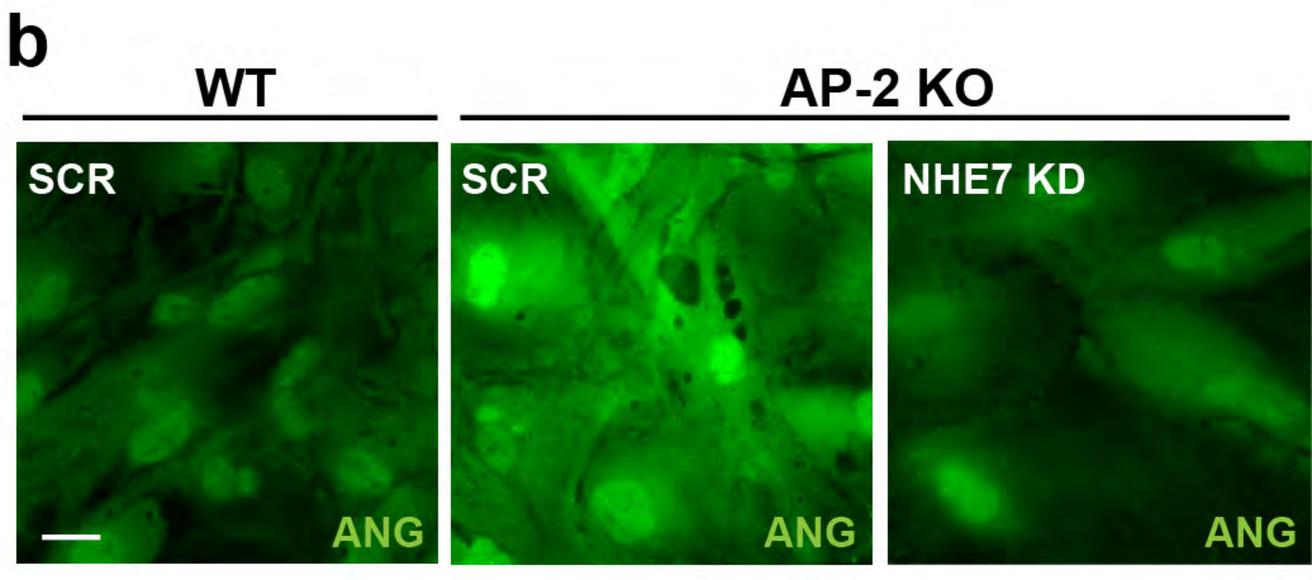


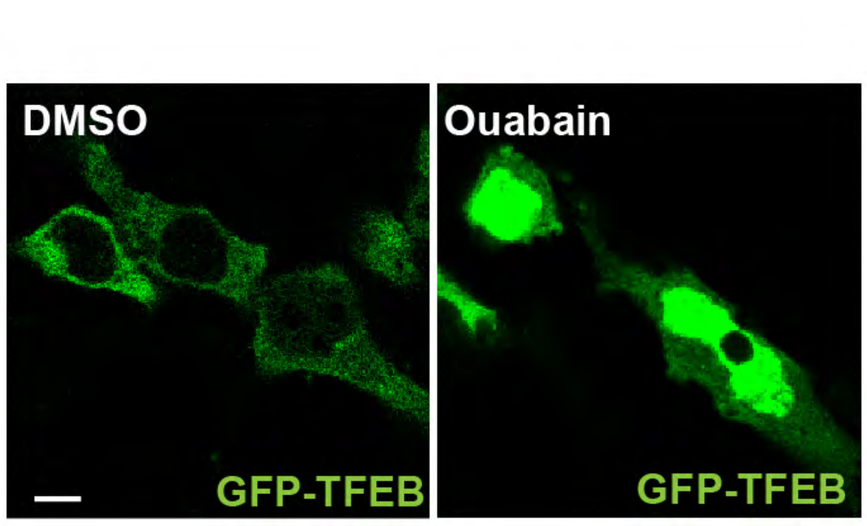


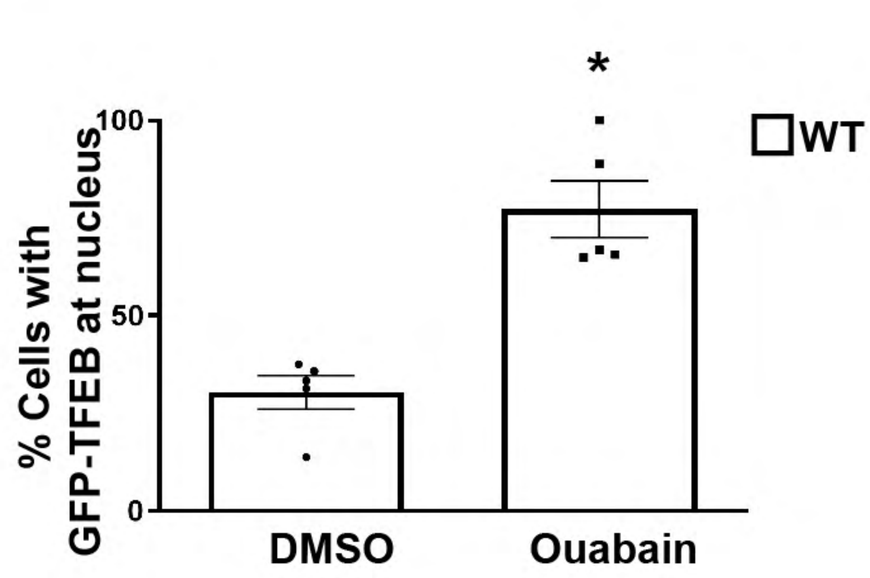


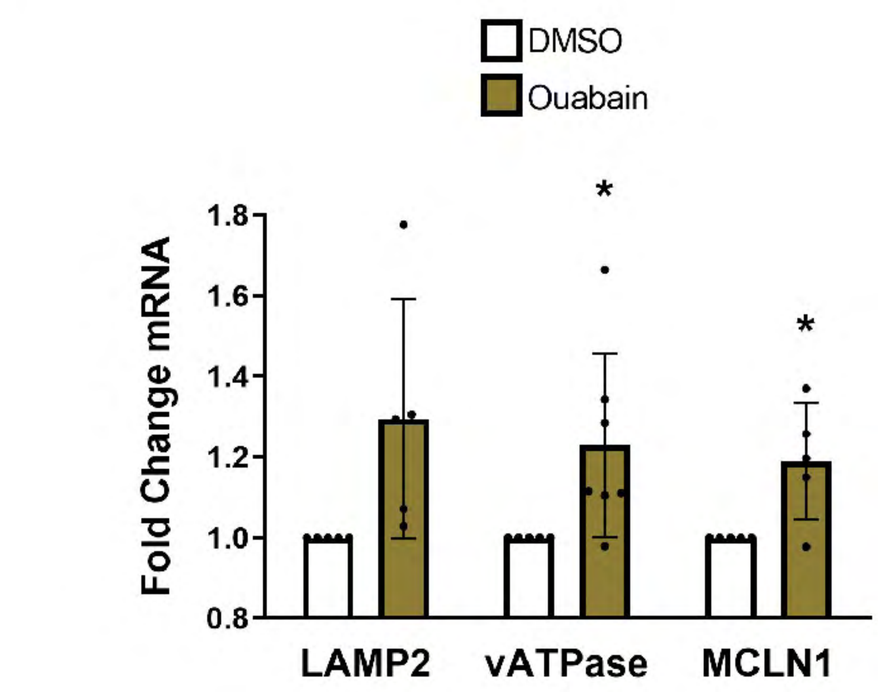


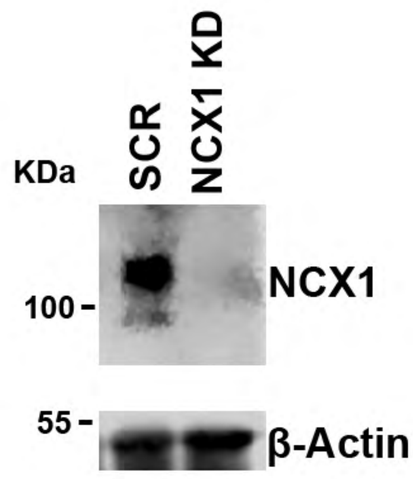


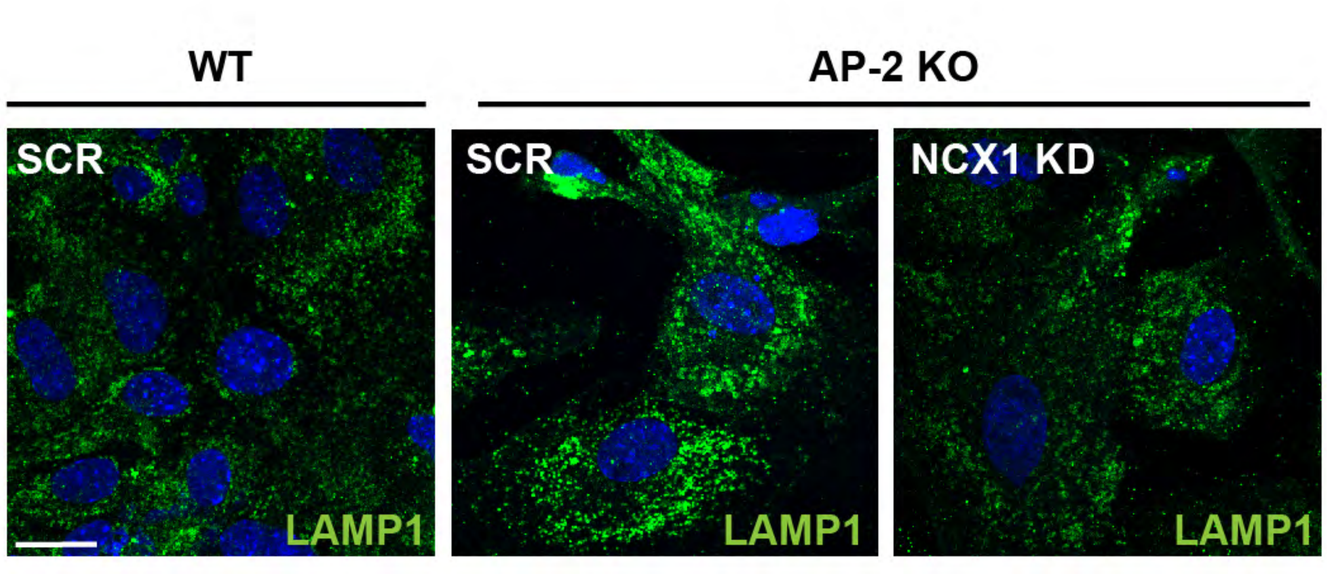


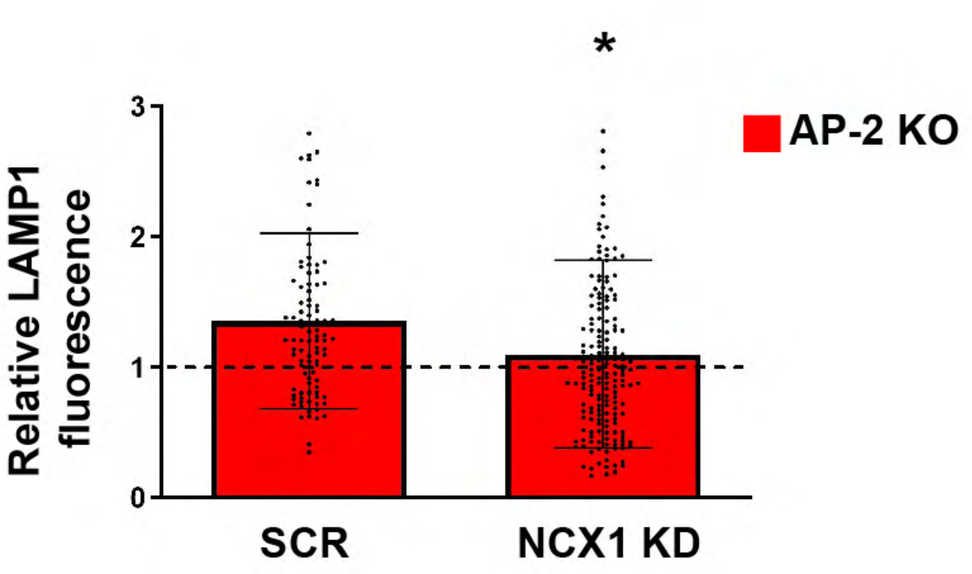

# Extended Data Fig. 9

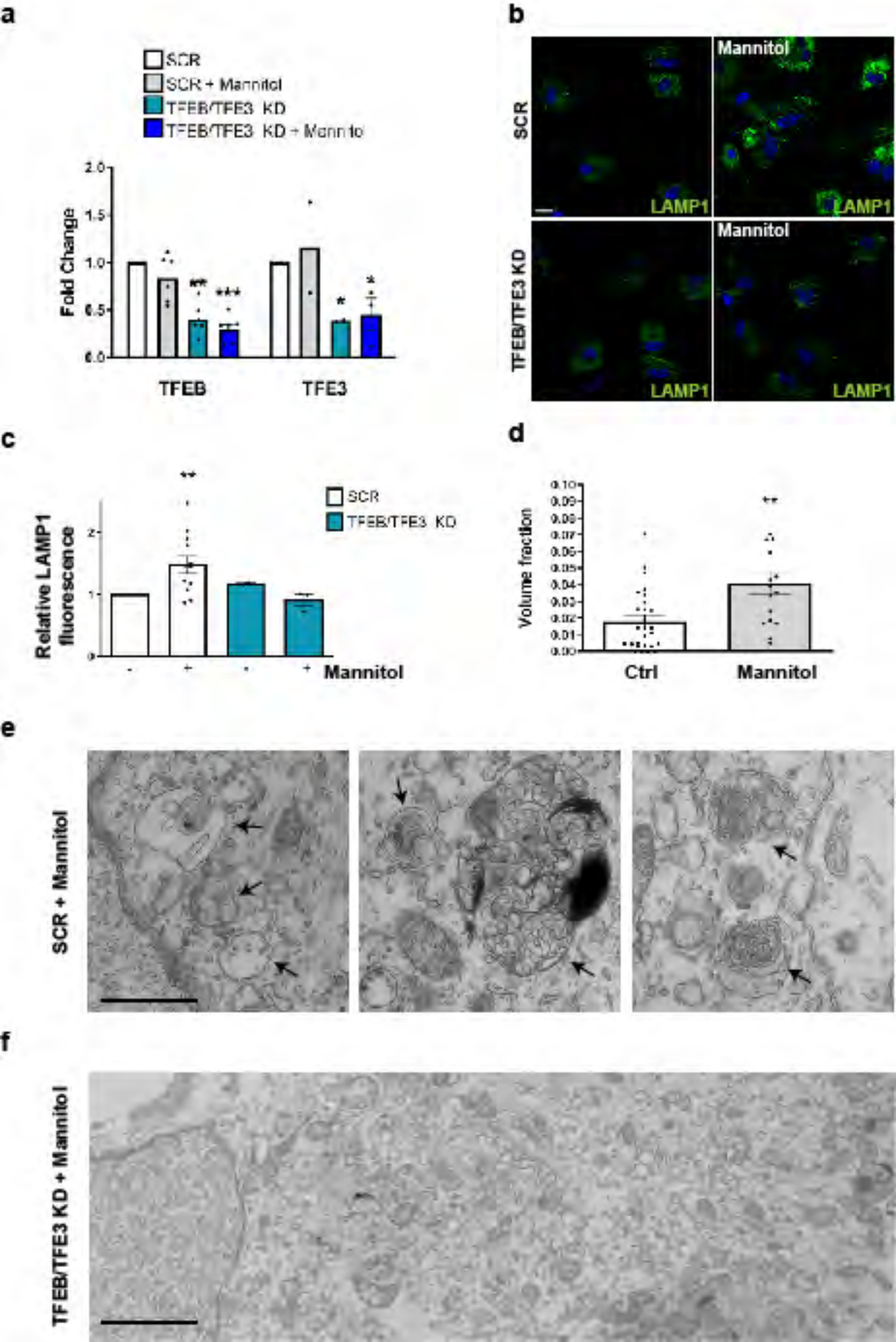

# Extended Data Fig. 10